Development of Functional Gas Diffusion Layers for use in CO_2 Reduction Reactors via Microscale Printing

2022 CNF REU Intern: Zeinab Ismail

Intern Affiliation: Physics, St. John's University

CNF REU Principal Investigator: Dr. Sadaf Sobhani, Mechanical and Aerospace Engineering, Cornell
CNF REU Mentor: Giancarlo D'Orazio, Mechanical and Aerospace Engineering, Cornell University

CNF REU Project and Primary Source(s) of Research Funding: 2022 Cornell NanoScale Science & Technology Facility Research Experiences for Undergraduates (CNF REU) Program via the National Science Foundation under Grant No. NNCI-2025233

Contact: z_nab01@hotmail.com, sobhani@cornell.edu, gd373@cornell.edu

Website: https://cnf.cornell.edu/education/reu/2022
Primary CNF Tools Used: NanoScribe GT2, Objet 30 Printer, AJA Sputter Deposition, Zeiss Ultra SEM

Abstract:

In a world reliant on the burning of fossil fuels to run some of its major industries, there is concern as to how we dispose of the carbon dioxide (CO_2) waste produced. One approach is to reprocess the CO_2 into simple hydrocarbons using a CO_2 Reduction Reactor (CO_2RR). A CO_2RR's ability to produce useful products relies heavily on its gas diffusion electrodes (GDEs), which consist of porous membranes called gas diffusion layers (GDLs) coated in a metal catalyst. GDLs act as a barrier against unwanted liquids, letting only gasses pass through.

A conventional GDE, consisting of PTFE and copper covered carbon paper, typically operates for a few hours before its efficiency begins to drop and it floods. Printing GDLs using a 3D printer would allow for optimization of the layer through the customization of the pore size, structure, and density of the layer.

Summary of Research:

The CO_2RR used consisted of three SLA-printed compartments: gas, anolyte, and catholyte compartments. The anode, ion-exchange membrane, and cathode used in the reactor were respectively a platinum mesh, nafion ion exchange membrane, and 3D printed GDL created using the NanoScribe GT2, attached to an adapter made by the Objet 30 printer, and sputtered in copper. The reactor was constantly being pumped with carbon dioxide gas and electrolytic solution, consisting of water and potassium bicarbonate. The process of creating functional GDLs was broken into three parts: designing a GDL, creating the gas diffusion electrode, and assembling the reactor and testing it.

The NanoScribe GT2 sweeps a femtosecond near IR laser across resin, curing sections with two-photon polymerization. The two resins experimented with to produce the GDLs were the IP-S and IP-Q resins. The general workflow for the NanoScribe consisted of creating a CAD model and generating an STL, slicing the STL using DeScribe, prepping the resist on a silicon wafer, loading the wafer into the printer, and printing, unloading, and developing the sample. The first design attempt to generate the full-scale layer of 10.095 mm × 10.095 mm × 400 µm thickness was too computationally intensive. The NanoScribe slicer, DeScribe, can work with files up to two gigabytes, but the full-scale GDL, in its lowest quality, was six gigabytes.

The next design created an STL out of 1/16 of the full-scale layer, one block, and used a for-loop of arrays and an overlap of 5 µm to build the full layer. The layer printed using this design began to deteriorate and peel off the silicon wafer after development. The final GDL design made and used was a 2 × 2 array of 5 mm × 5 mm × 100 µm each block, layered on top of each other four times, to create a thickness of 400 µm.

Using the IP-S resin and 2 × 2 array design, a second GDL print was made. After development, the GDL layers began to fall apart, and the layer began to peel off the wafer. At this point, the suitability of the IP-S resin was put in question.

The IP-S resin was initially chosen because it was not sensitive to overdevelopment and was the freshest resin available. It was only after printing the third gas diffusion using IP-Q resin instead that the layer turned out better than previous prints, with the IP-Q resin layer having no visible discoloration, excess uncured resin, or separation of layers from each other or off the wafer (see Figure 1).

After developing the layer in PGMEA for 45 minutes and IPA for 30 min, it was soaked for another 30 minutes in IPA. Next, it was sonicated for 10 minutes at 21°C, then placed on a hot plate of 90°C for 20 seconds and moved onto a cool plate. After doing this twice, the layer popped off the wafer.

Then the layer was glued to an adapter printed on the Objet 30 and cured using UV light. Afterwards, the glued pieces were sputtered with a 254 nm layer of copper, using the AJA sputter deposition tool (see Figure 2). Finally, the CO_2RR was assembled, and the finished gas diffusion electrode was incorporated into it (see Figure 3).

The CO_2RR was connected to a power source, potentiostat, and peristaltic pump. However, the gas chromatograph, a machine that would collect and quantify the gas products, was not working. The IR drop was collected and was found to be similar to an IR drop of a conventional GDL on the market. Then a cyclic voltammetry (CV) scan, which measures the change in current as different potentials are applied, was generated. Ideally, the plot should have multiple peaks, each peak representing the reduction/oxidation process. However, as shown in Figure 4, there's no current in the cell until about -1.2 V of potential is applied. This conclusion informs us that there is an electrochemical reaction taking place. However, there is another issue preventing a proper CV scan from being generated.

When the GDL was taken out of the cell, it was discovered that the copper wasn't adhering well to the GDL. A possible solution to try down the line would be to coat the layer initially with another metal, like chromium, then coat it with copper.

Conclusion and Future Steps:

Through the lengthy process of designing the gas diffusion layer, 3D printing it, and running it in a CO_2RR, we were able to produce a GDL that has a similar IR Drop to a conventional market GDL. More importantly, the GDL did not flood during the process of running the cell, showing the potential of using microscale manufacturing in producing optimized GDLs. The next steps would be to try coating the printed GDLs with a hydrophobic coating, as well sputtering it with chromium and copper. Afterwards, it would be tested in the CO_2RR when the gas chromatograph is working.

References:

[1] Energy Environ. Sci., 2021, 14, 3064 Wakerley, D., Lamaison, S., Wicks, J. et al. Gas diffusion electrodes, reactor designs and key metrics of low-temperature CO_2 electrolysers. Nat Energy 7, 130-143 (2022). https://doi.org/10.1038/s41560-021-00973-9.

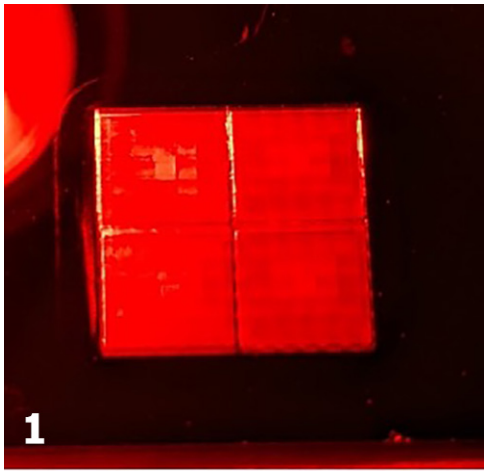

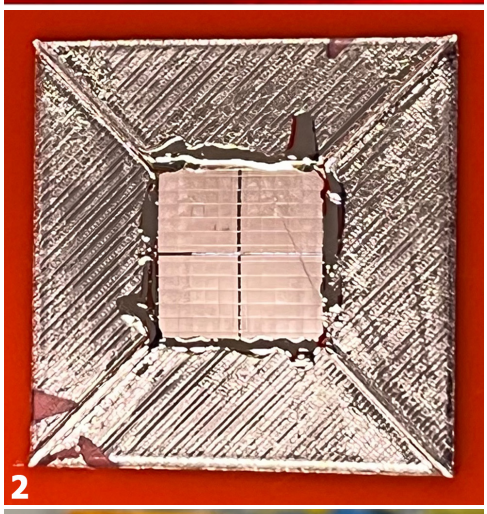

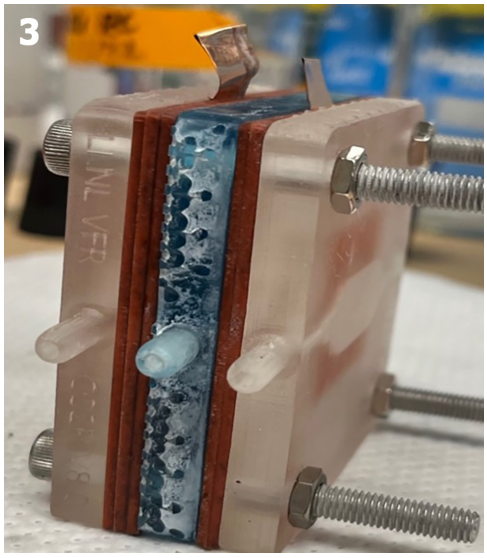

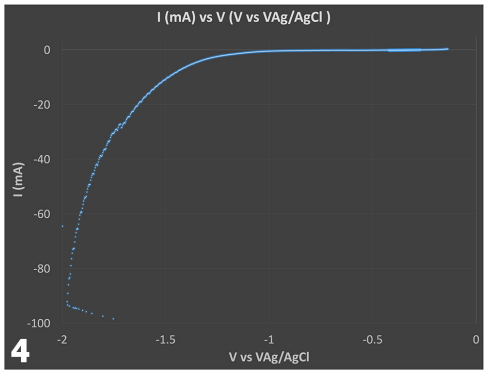

Figure 1, top: IP-Q resin layer with no visible discoloration, excess uncured resin, or separation of layers from each other or off the wafer. Figure 2, second from top: A 254 nm layer of copper was added using AJA sputter deposition. Figure 3, third from top: Assembled CO_2RR with gas diffusion electrode incorporated. Figure 4, bottom: Electrochemical reaction.

Anisotropic Gigahertz Antiferromagnetic Resonances of the Easy-Axis van der Waals Antiferromagnet CrSBr

CNF Project Number: 598-96

Principal Investigator: Daniel C. Ralph

User: Thow Min Jerald Cham

Affiliation: Laboratory of Atomic and Solid State Physics, Cornell University

Primary Source of Research Funding: National Science Foundation/Division of Materials Research, Air Force Office of Scientific Research, Agency for Science Technology and Research (Singapore)

Contact: dcr14@cornell.edu, tc676@cornell.edu

Primary CNF Tools Used: Supra SEM, Nabity Nanometer Pattern Generator, AJA Sputter Deposition, Even-Hour Evaporator

Abstract:

We report measurements of antiferromagnetic resonances in the van der Waals easy-axis antiferromagnet CrSBr. The spectra show good agreement with a Landau-Lifshitz model for two antiferromagnetically-coupled sublattices, accounting for inter-layer exchange and triaxial magnetic anisotropy. Fits allow us to quantify the parameters governing the magnetic dynamics: at 5K, the interlayer exchange field is $\mu_0 H_E$ = 0.395(2) T, and the hard and intermediate-axis anisotropy parameters are $\mu_0 H_c$ = 1.30(2) T and $\mu_0 H_a$ = 0.383(7) T [1].

Summary of Research:

Chromium bromide (CrSBr) is an A-type antiferromagnetic vdW semi-conductor with intralayer ferromagnetic coupling and interlayer antiferromagnetic coupling [2-4]. It has a bulk Néel temperature (T_N) of 132K and an intermediate ferromagnetic phase with Curie temperature (T_C) in the range of 164-185 K as measured using transport and optical methods [2,5,4]. Each vdW layer consists of two buckled rectangular planes of Cr and S atoms sandwiched between Br atoms. The layers are stacked along the *c*-axis through vdW interactions to form an orthorhombic structure (space group *Pmmn*). We investigate the antiferromagnetic resonances of CrSBr by placing the crystal on a coplanar waveguide and measuring the microwave absorption spectrum using a two-port vector network analyzer.

We align the crystal with its long axis perpendicular to the waveguide, such that the Néel axis is perpendicular to the in-plane RF field (H_{RF}). An external DC magnetic field is swept in-plane, either perpendicular, parallel, or at intermediate angles to the Néel axis. Representative transmission spectra as a function of applied field at 5K are shown in Figure 1. Dark green features represent

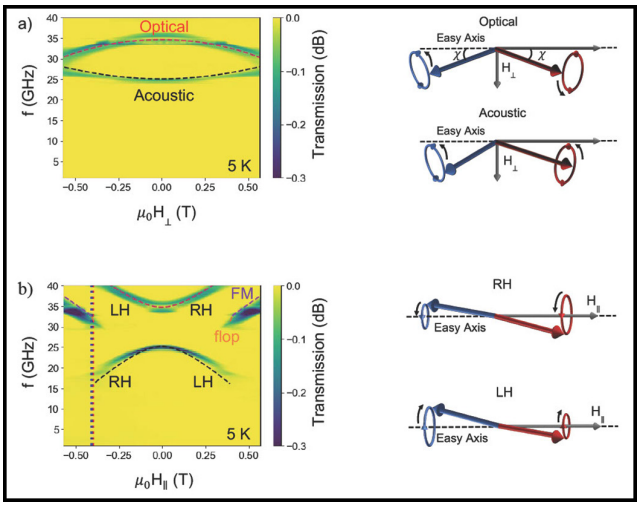

Figure 1: (a) Microwave transmission (S_{21}) signal as a function of $H_\perp$, magnetic field applied along the crystal a *axis. (b) The corresponding spectra as a function of H∥, magnetic field applied along the crystal* b *axis. S_{21} values are shown relative to a field-independent subtracted background. Dashed lines show a fit to the results of the L-L model. Diagrams on the right illustrate the form of some of the resonant modes.*

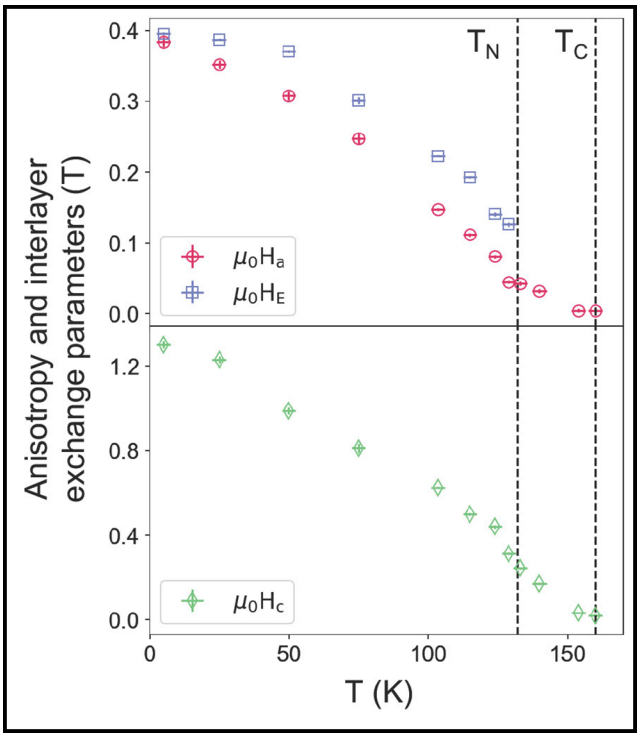

Figure 2: (a) Temperature dependence of the interlayer exchange H_E (blue squares) and the in-plane easy-axis anisotropy parameter H_a (red circles). (b) Temperature dependence of out-of-plane anisotropy parameter H_c. The black dashed lines indicate the estimated Néel temperature $T_N \approx 132$ K and the Curie temperature $T_c \approx 160$ K, previously measured in magnetometry and magnetotransport measurements.

strong microwave absorption due to resonance modes. We observe two resonance modes in the $H_\perp$ configuration and show their dependence on magnetic field in Figure 2a up to the maximum applied field of ± 0.57 T. We identify the two resonances in Figure 1a as acoustic and optical modes originating from an initial spin-flop configuration in which the two spin sublattices are canted away from the easy axis. In the $H_\parallel$ case (Figure 1b), two resonance features are also observed, but with opposite signs of concavity compared to Figure 1a.

Next, we investigate the evolution of the resonant modes with temperature. We observe qualitatively similar resonance features over the temperature range from 5 to 100 K. With increasing temperature, the modes shift to lower frequency and the magnetic field scales decrease for both the value of $H_\perp$ where the two modes become degenerate and for the value of $H_\parallel$ corresponding to the discontinuous transition. These observations can be attributed to decreasing values of all of the exchange and anisotropy parameters H_E, H_a and H_c with increasing temperature. Figure 2 plots the values of the parameters for a series of temperatures from 5 to 128K. We observe a monotonic decrease in all three parameters.

Conclusion and Future Steps:

In summary, we report measurements of gigahertz-frequency antiferromagnetic resonance modes in the van der Waals antiferromagnet CrSBr that are anisotropic with regard to the angle of applied magnetic field relative to the crystal axes. The modes are well described by two coupled Landau-Lifshitz equations for modeling the spin sublattices, when one accounts for interlayer exchange and triaxial magnetic anisotropy present in CrSBr. Our characterization of antiferromagnetic resonances in an easily-accessible frequency range, and the understanding of how the resonances can be tuned between uncoupled and strongly-coupled by adjusting magnetic field, sets the stage for future experiments regarding manipulation of the modes and the development of capabilities like antiferromagnetic spin-torque nano-oscillators.

References:

[1] Thow Min Jerald Cham, Saba Karimeddiny, Avalon H. Dismukes, Xavier Roy, Daniel C. Ralph, and Yunqiu Kelly Luo. Anisotropic gigahertz antiferromagnetic resonances of the easy-axis van der waals antiferromagnet crsbr. Nano Letters, 22(16):6716-6723, 2022. PMID: 35925774.

[2] Evan J. Telford, Avalon H. Dismukes, Kihong Lee, Minghao Cheng, Andrew Wieteska, Amymarie K. Bartholomew, Yu-Sheng Chen, Xiaodong Xu, Abhay N. Pasupathy, Xiaoyang Zhu, Cory R. Dean, and Xavier Roy. Layered antiferromagnetism induces large negative magnetoresistance in the van der waals semiconductor CrSBr. Advanced Materials, 32(37):2003240, 2020.

[3] Ke Yang, Guangyu Wang, Lu Liu, Di Lu, and Hua Wu. Triaxial magnetic anisotropy in the two-dimensional ferromagnetic semiconductor crsbr. Physical Review B, 104:144416, Oct 2021.

[4] Evan J Telford, Avalon H Dismukes, Raymond L Dudley, Ren A Wiscons, Kihong Lee, Daniel G Chica, Michael E Ziebel, Myung-Geun Han, Jessica Yu, Sara Shabani, Allen Scheie, Kenji Watanabe, Takashi Taniguchi, Di Xiao, Yimei Zhu, Abhay N Pasupathy, Colin Nuckolls, Xiaoyang Zhu, Cory R Dean, and Xavier Roy. Coupling between magnetic order and charge transport in a two-dimensional magnetic semi.conductor. Nature Materials, 21(7):754-760, 2022.

[5] Kihong Lee, Avalon H. Dismukes, Evan J. Telford, Ren A. Wiscons, Jue Wang, Xiaodong Xu, Colin Nuckolls, Cory R. Dean, Xavier Roy, and Xiaoyang Zhu. Magnetic Order and Symmetry in the 2D Semiconductor CrSBr. Nano Letters, 21(8):3511-3517, 2021.

Gate-Tunable Anomalous Hall Effect in a 3D Topological Insulator/2D Magnet van der Waals Heterostructure

CNF Project Number: 598-96

Principal Investigator(s): Daniel C. Ralph

User(s): Rakshit Jain, Vishakha Gupta

Affiliation(s): Physics Department, Cornell University

Primary Source(s) of Research Funding: Air Force Office of Scientific Research, Department of Energy

Contact: dcr14@cornell.edu, rj372@cornell.edu, vg264@cornell.edu

Primary CNF Tools Used: Zeiss Supra SEM, Nabity Nanometer Pattern Generator, AJA Sputter Deposition, CVC SC4500 Even-Hour Evaporator

Abstract:

We demonstrate advantages of samples made by mechanical stacking of exfoliated van der Waals materials for controlling the topological surface state of a 3-dimensional topological insulator (TI) via interaction with an adjacent magnet layer. We assemble bilayers with pristine interfaces using exfoliated flakes of the TI $BiSbTeSe_2$ and the magnet $Cr_2Ge_2Te_6$, thereby avoiding problems caused by interdiffusion that can affect interfaces made by top-down deposition methods. The samples exhibit an anomalous Hall effect (AHE) with abrupt hysteretic switching. For the first time in samples composed of a TI and a separate ferromagnetic layer, we demonstrate that the amplitude of the AHE can be tuned via gate voltage with a strong peak near the Dirac point. This is the signature expected for the AHE due to Berry curvature associated with an exchange gap induced by interaction between the topological surface state and an out-of-plane-oriented magnet.

Summary of Research:

Interactions between three-dimension topological insulators (TIs) and magnets can induce exotic topological phases like the quantum anomalous Hall or axion insulator states, and might be used to harness the properties of topological-insulator surface states in spintronic devices [1]. We study TI/magnet bilayers using an all-van der Waals (vdW) heterostructure, by stacking together in a glovebox exfoliated flakes of the TI $BiSbTeSe_2$ and the insulating magnet $Cr_2Ge_2Te_6$ [2].

In contrast to previous work on TI/magnet samples grown by top-down deposition methods, or made by assembling exfoliated flakes with air exposure, the use of a glovebox-assembled vdW structure ensures a defect- and diffusion-free atomically-flat interface. Further, our use of a thin insulating vdW magnet enables both spatially-uniform magnetic coupling to the topological surface state and large tunability of the electron chemical potential using electrostatic gating (see Figure 1 for device structure and gating geometry). We measure the anomalous Hall response while continuously controlling the contribution of the surface state by gating.

The out-of-plane magnetization of the CGT is expected to break time-reversal symmetry in the BSTS surface through proximity coupling and result in the opening of an exchange gap (Δ) in the adjacent Dirac surface state, as described by the following 2D Dirac Hamiltonian:

$$H(k) = \hbar v_F(k_x\sigma_y - k_y\sigma_x) + \Delta\sigma_z$$

where $\sigma_{x,y,z}$ are the Pauli spin matrices, k_x and k_y are in-plane wave vectors, and v_F is the Fermi velocity. States in the vicinity of the gap have non-zero Berry curvature, with equal and opposite values on opposite sides of the gap. Therefore when states on opposite sides of the gap have unequal occupations, the result is a nonzero Hall conductance, σ_{xy}. The peak value of the Hall conductance, when the electron chemical potential lies in the gap, should be $e^2/2h$ in the low temperature limit (3). Consequently, a peak of the Hall resistivity ($\rho_{xy} = \sigma_{xy}/(\sigma^2_{xx} + \sigma^2_{xy})$), where σ_{xx} is the longitudinal conductivity) should be found when the chemical potential is tuned through the gap.

In Figure 2a, we show the Hall resistance (R_{xy}) after subtraction of the ordinary Hall background for the measurement done at top gate voltage V_{tg} = 0V. The measurements are performed at 4.4K and under a constant bias current, with the bottom-gate voltage V_{bg} fixed at 0V. The current flows primarily through the BSTS layers since CGT is insulating at this temperature. We observe hysteretic step-like changes in V_{xy} corresponding to an anomalous Hall effect (AHE), indicative of a strong perpendicular anisotropy for the magnetism in CGT that is coupled to the BSTS surfaces.

As the chemical potential of the top surface is tuned by varying the V_{tg}, we observe a modulation in the observed AHE signal. The amplitude of the AHE response is maximum at V_{tg} = 0.55V and becomes smaller as the gate voltage is tuned on either side of this maximum.

In Figure 2b, we plot the extracted signal size of the anomalous Hall resistance response as a function of V_{tg} (black trace). This trend tracks approximately with the gating behaviour of the longitudinal resistance R_{xx} shown by the dotted blue trace. We therefore identify the maximum in the AHE response as due to tuning of the electron chemical potential within the exchange gap, as expected from the Berry curvature picture.

Conclusions and Future Directions:

We have demonstrated that the use of mechanical assembly of van der Waals materials to form a pristine interface provides a strategy that avoids materials challenges which have inhibited research progress in studying topological insulator/magnet heterostructures grown by molecular beam epitaxy or other deposition techniques. The high quality of mechanically-assembled van der Waals structures provides a platform for future studies of the quantum anomalous Hall and axion insulator states, and the rich phenomenology of topological magneto-electric phenomena predicted for these states.

References:

[1] Tokura, Y., Yasuda, K., and Tsukazaki, A. Magnetic topological insulators. Nature Reviews Physics 1, 126–143 (2019).

[2] Gupta, V., et al. Gate-tunable anomalous Hall effect in a 3D topological insulator/2D magnet van der Waals heterostructure. Nano Letters URL https://doi.org/10.1021/acs.nanolett.2c02440.

[3] Xiao, D., Chang, M.-C. and Niu, Q. Berry phase effects on electronic properties. Rev. Mod. Phys. 82, 1959 (2010).

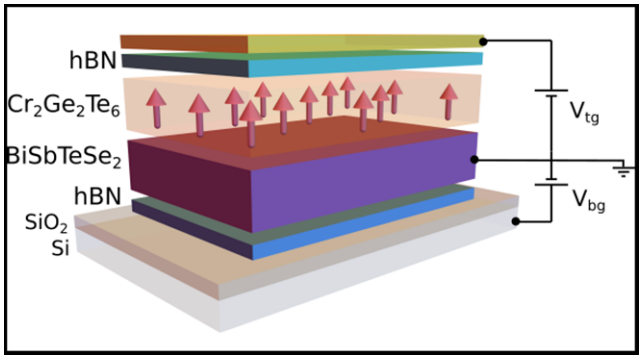

Figure 1: Schematic of the device geometry and electrostatic gating geometry. TI and 2D magnet flakes with few-layer thickness are double-encapsulated between h-BN layers on a Si/SiO_2 substrate.

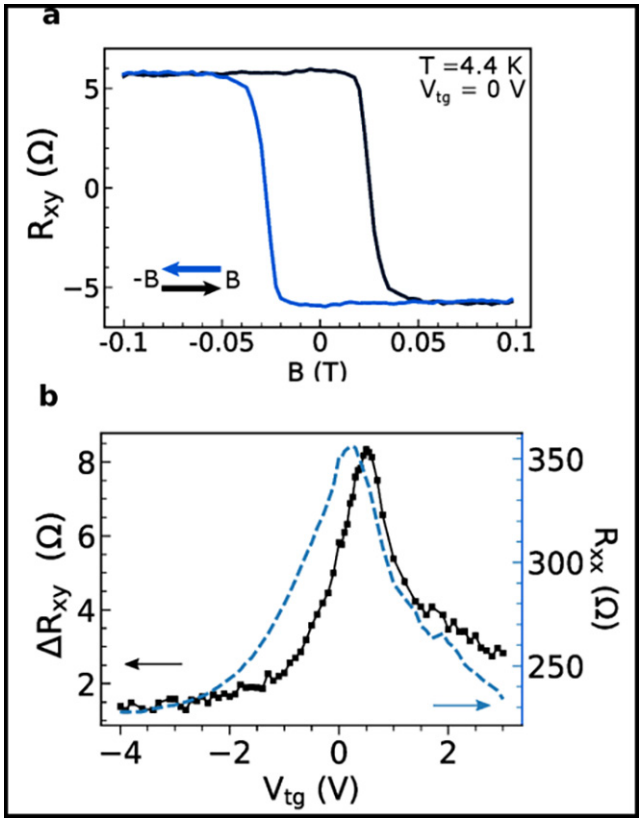

Figure 2: (a) AHE contribution to R_{xy} at V_{tg} = 0 after subtraction of linear background. (b) Size of AHE signal (black solid line) ΔR_{xy} as a function of top-gate voltage. The trend matches closely with the observed top-gate dependence of R_{xx} (blue dashed line) measured at zero magnetic field.

Fabricating Micron-Sized Devices for Measuring Magnetic Properties

CNF Project Number: 598-96

Principal Investigator(s): Daniel C. Ralph

User(s): Maciej Olszewski

Affiliation(s): Laboratory of Atomic and Solid State Physics (LASSP), Cornell University

Primary Source(s) of Research Funding: Defense Advanced Research Projects Agency (DARPA), National Science Foundation (NSF)

Contact: dcr14@cornell.edu, mwo34@cornell.edu
Website: https://ralphgroup.lassp.cornell.edu/

Primary CNF Tools Used: Zeiss Supra SEM, Nabity Nanometer Pattern Generator System, SC4500 Odd-Hour / Even-Hour Evaporator, Oxford 81 Etcher, AFM – Veeco Icon

Abstract:

We present various methods for improving the removal of residual polymethyl methacrylate (PMMA) resist in electron beam lithography (EBL) processes. We explore various methods of PMMA removal, including furnace annealing, plasma cleaning, solvent stripping, and atomic force microscope (AFM) tip cleaning. We compare the various removal procedures by measuring the average roughness of the region using AFM. We report that the best method for removing polymer residue is a combination of solvent stripping and AFM tip cleaning.

Summary of Research:

Van der Waals material heterostructures fabricated from exfoliated crystals have atomically smooth layers, forming pristine interfaces between various materials [1]. This allows for studying new and exotic states of matter as well as improving the understanding of physics in the quantum mechanics regime. One drawback of this technique is the different shapes and sizes of the exfoliated flakes, which compose the heterostructures. Especially in the case of geometrically sensitive measurements, such as Hall conductance, we require a very precise device geometry.

This issue can be resolved by a combination of lithography, etching and metal deposition, however these techniques usually involve various polymers which can contaminate the pristine nature of the interfaces, reduce the electrical mobility in the materials, and introduce noise in the measurements. To try and maintain a pristine nature of the interfaces we explore a various combination of methods that can help clean the residual resist from the materials. We explore various methods presented in literature, including furnace annealing [2], plasma cleaning [3], various solvent stripping [4,5], and AFM tip cleaning [6].

Initially, we tried using various forms of vacuum furnace annealing and plasma cleaning to remove the remainder polymer residue. These tests however an increase of black spots on the devices which has be reported to be residual amorphous carbon atoms [2,3]. We then turned to trying various wet solvent stripping methods using various combinations of acetone, dichloromethane, glacial acetic acid, and Allresist AR700-61.

For each process we ran the same e-beam lithography process on the Nabity Nanometer Pattern Generator System (NPGS) using a polymethyl methacrylate (PMMA) bilayer resist, after developing we either etched the devices using the Oxford 81 Etcher or deposited metal using the SC4500 Odd-Hour Evaporator. After the etching and/or metal deposition the devices were soaked in various solvents for varying amounts of

Process Type	RMS Roughness (pm)	Mean Roughness (pm)
Allresist	367.05	303.23
DCM and Acetone	632.43	426.76
Toluene	3047.25	2237.50
Acetone	649.40	524.50
Acetic Acid	1150.23	900.01

Figure 1: Table of the surface roughness of the device region after stripping in various resists. The values are obtained by measuring the roughness across many devices.

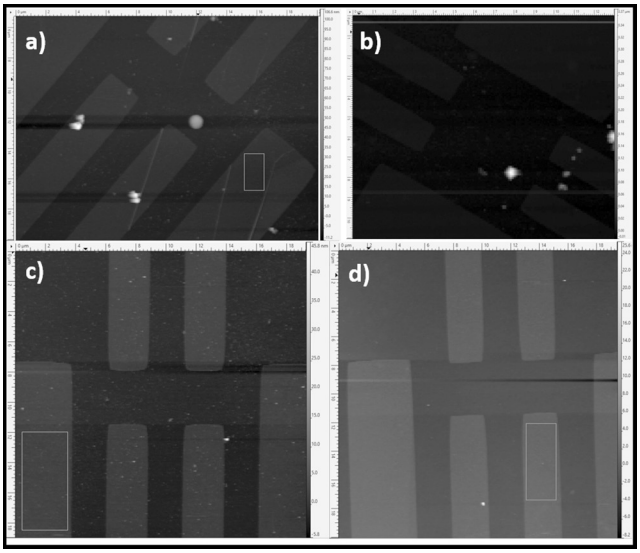

Figure 2: An AFM topography scan of a sample device after a) acetone stripping, b) acetone/dichloromethane stripping, c) acetic acid stripping, d) acetone/Allresist stripping.

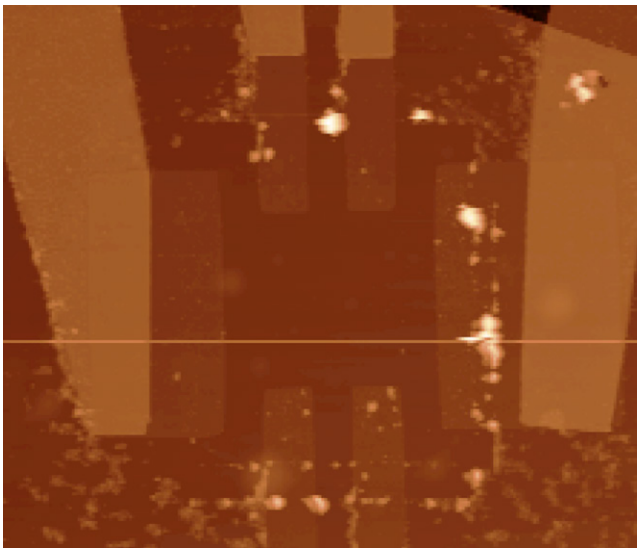

Figure 3: An AFM topography scan of a sample device after the AFM tip cleaning procedure done after acetone stripping.

time. The roughness of the devices was then measured using tapping mode AFM, sample scans for various solvents are shown in Figure 1. Further we analyzed the roughness for various regions and complied the average roughness value for different solvent methods in Figure 2. We were able to conclude that soaking in Allresist was the best solvent at removing PMMA residue from the device areas.

Finally, we attempted to clean the devices using an AFM tip. This was done by taking an AFM tip in contact mode and dragging it over the surface of the device moving the PMMA residue around. As shown in Figure 3 this causes the PMMA residue to move around however it does not remove the resist but simply relocates it to a different region on the chip. This process proved to be by far the best, often yielding roughness of less than 300 pm.

In summary, we showed that using various solvents for stripping can improve the removal of residual PMMA, however AFM tip cleaning is by far the most efficient method of removing the polymer.

This research allowed us to determine the most optimal method of removing the residue from our devices and improving the interfaces in the heterostructures.

References:

[1] Castellanos-Gomez, A., Duan, X., Fei, Z. et al. Van der Waals heterostructures. Nat Rev Methods Primers 2, 58 (2022).

[2] Wang, X., et al. Direct Observation of Poly (Methyl Methacrylate) Removal from a Graphene Surface. Chem Mater 29, 5 (2017).

[3] Cunge, G., et al. Dry efficient cleaning of poly-methyl-methacrylate residues from graphene with high density H_2 and H_2-N_2 plasmas. Journal of Applied Physics 118, 12 (2015).

[4] Honghwi P., et al. Optimized poly (methyl methacrylate)-mediated graphene-transfer process for fabrication of high-quality graphene layer. Nanotechnology 29, 415303 (2018).

[5] Tyagi, A., et al. Ultra-clean high-mobility graphene on technologically relevant substrates. Nanoscale, 14, 2167 (2022).

[6] Chen, S., et al. Tip-Based Cleaning and Smoothing Improves Performance in Monolayer MoS_2 Devices. ACS Omega 6, 5 (2021).

Nanofabricated Superconducting Devices for Vortex Dynamics and Qubits

CNF Project Number: 1314-05

Principal Investigator(s): Britton L.T. Plourde

User(s): Brad Cole, Kenneth Dodge, Jaseung Ku, Clayton Larson, Yebin Liu, Eric Yelton

Affiliation(s): Department of Physics, Syracuse University

Primary Source of Research Funding: Army Research Office

Contact: bplourde@syr.edu, bgcole@syr.edu, krdodgej@syr.edu, jku102@syr.edu, cllarson@syr.edu, yliu166@syr.edu, epyelton@syr.edu
Website: https://bplourde.expressions.syr.edu/

Primary CNF Tools Used: ASML Photostepper, JEOL 6300, Plasma-Therm 770

Abstract:

We fabricate superconducting microwave devices for studying the dynamics of vortices at low temperatures and for forming novel qubits. Vortices are quantized bundles of magnetic flux that thread many different superconductors over a particular range of applied magnetic field. By using disordered superconducting thin films to form high kinetic inductance wires combined with novel arrays of Josephson junctions, we are able to build structures that can lead to qubits that are protected against decoherence. With charge-sensitive superconducting qubits, we are able to probe sources of correlated errors in quantum processors.

Summary of Research:

Superconducting microwave circuits play an important role in quantum information processing. Circuits composed of Josephson junctions and capacitors with superconducting electrodes can serve as qubits, the fundamental element of a quantum computing architecture. Various loss mechanisms limit the ultimate performance of these devices, including trapped magnetic flux vortices. Vortices can be trapped in the superconducting electrodes when background magnetic fields are present and contribute dissipation when driven with microwave currents [1]. Thus, techniques for controlling the trapping of vortices are critical to the development of large-scale quantum information processors with superconducting circuits.

By arranging nanoscale Al-AlO_x-Al Josephson tunnel junctions in novel arrays, it is possible to implement new qubit designs that are protected against decoherence [2-4]. We are also able to use such Al-AlO_x-Al tunnel

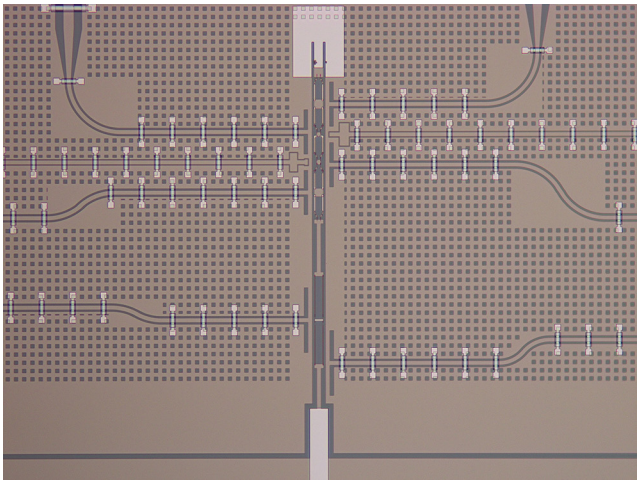

Figure 1: Optical micrograph of plaquette structures formed from arrays of Al-AlO_x-Al Josephson junctions for protected qubit design with Nb ground plane and flux-and charge-bias lines along with Al/SiO_x ground straps.

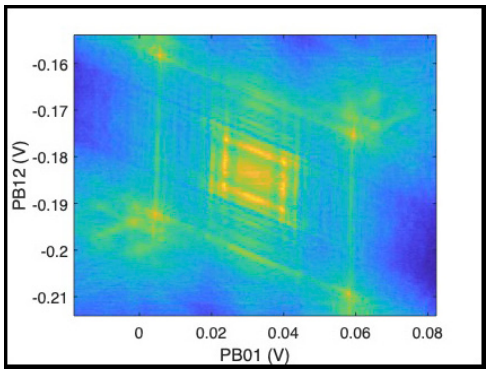

Figure 2: Microwave transmission through feedline coupled to readout cavity with capacitive coupling to plaquette-chain structure as a function of the magnetic flux bias using two of the on-chip bias lines.

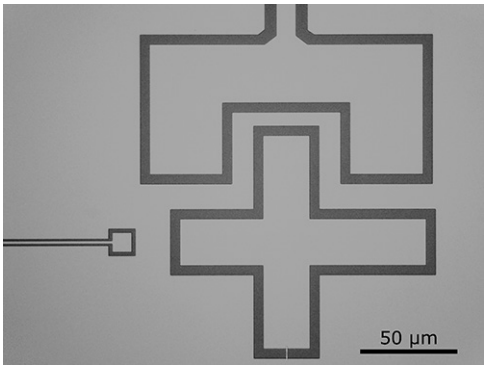

Figure 3: Optical micrograph of charge-sensitive transmon qubit with Al-AlO$_x$-Al tunnel junction for measurement of phonon-mediated quasiparticle poisoning.

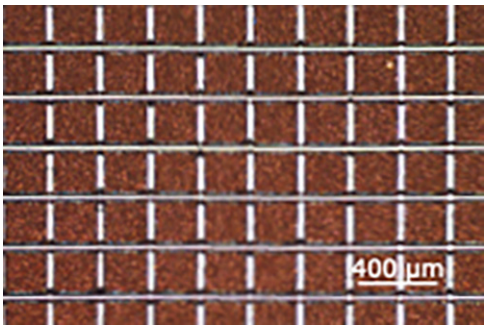

Figure 4: Optical micrograph of electroplated Cu islands on the back side of Si chip for downconversion of high energy phonons, with transmon qubits on the device layer.

junctions in superconducting qubits to probe poisoning effects from nonequilibrium quasiparticles, which are a source of correlated errors in quantum processors. We can mitigate this quasiparticle poisoning through the use of electroplated Cu metallic reservoirs for downconversion of high energy phonons [5].

We fabricate our microwave resonators from various superconducting films, including aluminum and niobium, deposited onto silicon wafers in vacuum systems at Syracuse University. We define the patterns on the ASML stepper and transfer them into the films with a combination of reactive ion etching and liftoff processing. For defining Josephson junctions, we use the JEOL 6300 along with a dedicated deposition system at Syracuse University. We measure these circuits at temperatures of 100 mK and below in our lab at Syracuse University.

References:

[1] Song, C., Heitmann, T.W., DeFeo, M.P., Yu, K., McDermott, R., Neeley, M., Martinis, John M., Plourde, B.L.T.; "Microwave response of vortices in superconducting thin films of Re and Al"; Physical Review B 79, 174512 (2009).

[2] Doucot, B., Ioffe, L.; "Physical implementation of protected qubits"; Reports on Progress in Physics 75, 072001 (2012).

[3] Liu, Y., Dodge, K., Cole, B., Ku, Shearrow, A., Snyder, M., Brann, E., Klots, A., Faoro, L., Ioffe, L.B., McDermott, R., Plourde, B.; "Charge-parity qubits based on concatenation of p-periodic Josephson elements: Part 1"; Bull. Am. Phys. Soc. 2022, https://meetings.aps.org/Meeting/MAR22/Session/S41.6

[4] Dodge, K., Liu, Y., Cole, B., Ku, Shearrow, A., Snyder, M., Brann, E., Klots, A., Faoro, L., Ioffe, L.B., McDermott, R., Plourde, B.; "Charge-parity qubits based on concatenation of p-periodic Josephson elements: Part 2"; Bull. Am. Phys. Soc. 2022, https://meetings.aps.org/Meeting/MAR22/Session/S41.5

[5] Iaia, V., Ku, J., Ballard, A., Larson, C.P., Yelton, E., Liu, C.H., Patel, S., McDermott, R., Plourde, B.L.T.; "Phonon downconversion to suppress correlated errors in superconducting qubits"; arxiv:2203.06586 (2022).

Fabrication of Nanoscale Josephson Junctions for Quantum Coherent Superconducting Circuits

CNF Project Number: 1735-08

Principal Investigator(s): Britton L.T. Plourde

User(s): Brad Cole, Tianna McBroom, JT Paustian, Michael Senatore

Affiliation(s): Department of Physics, Syracuse University

Primary Source(s) of Research Funding: Air Force Research Lab,
Air Force Office of Scientific Research

Contact: bplourde@syr.edu, bgcole@syr.edu, tamcbroo@syr.edu,
jtpausti@syr.edu, masenato@syr.edu
Website: https://bplourde.expressions.syr.edu/

Primary CNF Tools Used: ASML Photostepper, JEOL 6300, Plasma-Therm 770

Abstract:

We fabricate nanoscale superconductor tunnel junctions and other structures for experiments involving quantum coherent circuits. Such circuits have shown great promise in recent years for explorations of quantum mechanics at the scale of circuits on a chip and for forming qubits, the foundational elements of a quantum computer. The quantum state of these superconducting qubits can be manipulated with microwave radiation at low temperatures. We are currently developing superconducting metamaterial structures with novel microwave mode spectra for coupling to superconducting qubits.

Summary of Research:

The unique properties of nanoscale Josephson junctions enable a wide range of novel superconducting circuits for investigations in many diverse areas. In recent years, circuits composed of such junctions have emerged as promising candidates for the element of a quantum computer, due to the low intrinsic dissipation from the superconducting electrodes and the possibility of scaling to many such qubits on a chip [1]. The quantum coherent properties of the circuits are measured at temperatures below 50 mK with manipulation of the qubit state through microwave excitation.

We are developing multimode microwave resonators using combinations of superconducting lumped-circuit elements to engineer metamaterial transmission lines, including metamaterial ring resonator devices. These structures exhibit novel mode structures characteristic of left-handed materials [2]. We are fabricating such metamaterial transmission lines from Al and Nb films on Si and characterizing these at low temperatures [2]. We are working on experiments to couple these left-handed lines and ring resonators to superconducting qubits for experiments involving the exchange of microwave photons [2-4].

We pattern these circuits at the CNF with nanoscale structures defined with electron-beam lithography on the JEOL 6300 integrated with photolithographically defined large-scale features. The junctions are fabricated using the standard double-angle shadow evaporation technique, in which a resist bilayer of copolymer and PMMA is used to produce a narrow PMMA airbridge suspended above the substrate. Evaporation of aluminum from two different angles with an oxidation step in between forms a small Al-AlO_x-Al tunnel junction from the deposition shadow of the airbridge. We have developed a process for defining these junctions with electron-beam lithography and we perform the aluminum evaporations in a dedicated chamber at Syracuse. We pattern large-scale features using the ASML stepper, with electron-beam evaporation of Al and sputter-deposition of Nb. Measurements of these circuits are performed in cryogenic systems at Syracuse University, including dilution refrigerators for achieving temperatures below 30 mK.

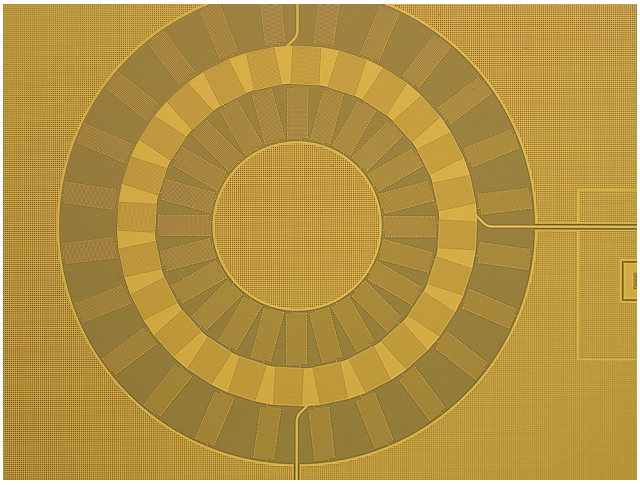

Figure 1: Optical micrograph of left-handed metamaterial ring resonator fabricated from Nb on Si.

Figure 2: Zoomed-in optical micrograph of transmon qubit coupled to metamaterial ring resonator.

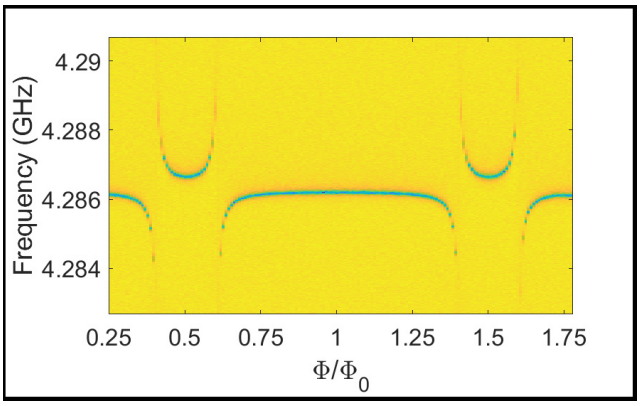

Figure 3: Measurement of microwave transmission through feedline coupled to metamaterial ring resonator as a function of the magnetic flux bias to the transmon qubit. Vacuum Rabi splittings in spectrum are characteristic of quantum mechanical coupling between qubit and ring resonator.

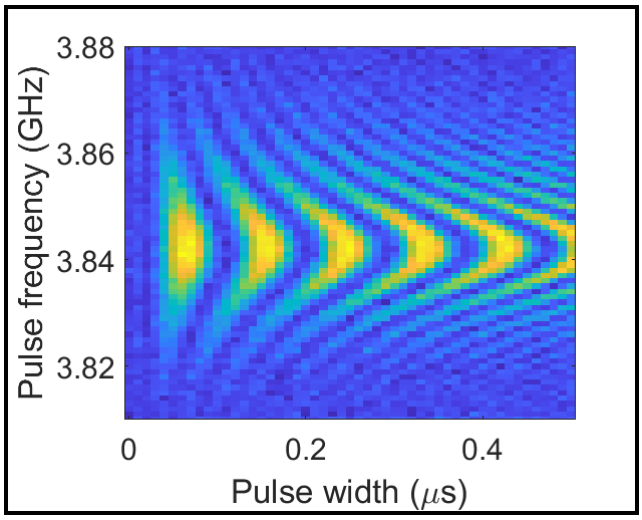

Figure 4: Measurement of Rabi oscillations of transmon qubit coupled to metamaterial ring resonator as a function of microwave drive frequency and pulse duration.

References:

[1] Clarke, J. and Wilhelm, F.K.; "Superconducting quantum bits"; Nature, 453, 1031 (2008).

[2] Wang, H., Zhuravel, A., Indrajeet, S., Taketani, B., Hutchings, M., Hao, Y., Rouxinol, F., Wilhelm,F., LaHaye, M.D., Ustinov, A., Plourde, B.; "Mode Structure in Superconducting Metamaterial Transmission Line Resonators"; Physical Review Applied 11, 054062 (2019).

[3] Indrajeet, S., Wang, H., Hutchings, M.D., Taketani, B.G., Wilhelm, F.K., LaHaye, M.D., Plourde, B.L.T.; "Coupling a Superconducting Qubit to a Left-Handed Metamaterial Resonator"; Physical Review Applied 14, 064033 (2020).

[4] McBroom, T.A., Ku, J., Cole, B.G., Plourde, B.; "Characterization of left-handed metamaterial ring resonator coupled to transmon qubits"; Bull. Am. Phys. Soc. 2022, http://meetings.aps.org/Meeting/MAR22/Session/Q37.3.

Probing Nanoscale Magnetism in 2D van der Waals Ferromagnet $Fe5GeTe_2$ with Magneto-Thermal Microscopy

CNF Project Number: 2091-11

Principal Investigator(s): Gregory D. Fuchs

User(s): Eegene (Clara) Chung

Affiliation(s): Department of Physics, School of Applied and Engineering Physics; Cornell University

Primary Source(s) of Research Funding: Air Force Office of Scientific Research (AFOSR) Multidisciplinary Research Program of the University Research Initiative (MURI) Grant (FA9550-18-1-0480)

Contact: gdf9@cornell.edu, ec893@cornell.edu

Primary CNF Tools Used: GCA 6300 DSW 5X g-line Wafer Stepper, AJA Orion Sputtering Systems, DISCO Dicing Saw, Heidelberg Mask Writer – DWL2000, Westbond 7400A Ultrasonic Wire Bonder

Abstract:

The relevant length and time scales of magnetic phenomena are typified by the width of domain walls, ranging over 10-1000 nm, and the time scale of ferromagnetic resonance and spin waves, ranging over 10-1000 ps. Currently, synchrotron x-ray techniques are the only reliable methods capable of simultaneously resolving both spatial and temporal scales. However, they are facility techniques that impose a limit on its accessibility and throughput. Here, we present a table-top method called magneto-thermal microscopy [1], to study magnetism with a spatial resolution of 650 nm (≤ 100 nm with near-field methods [2]) and a temporal resolution of 10-100 ps. This technique is based on the magneto-thermoelectric anomalous Nernst effect for conducting magnetic materials. The spatial resolution is limited only by the area of the thermal excitation, and it possesses no fundamental limit due to diffraction. We present a study of the recently discovered two-dimensional ferromagnetic van der Waals metal Fe_5GeTe_2 [3] using magneto-thermal microscopy to image the static magnetization at low temperatures. This work is part of an ongoing effort using magneto-thermal interactions to probe the competition between spin and charge ordered phases of this material, along with associated changes in band structure [4].

Summary of Research:

Two-dimensional (2D) magnets are interesting for applications in spintronics, in part because of their low-energy switching of spin states through various gating methods and ability to create heterostructures with engineered properties [5]. They are also interesting for their exotic quantum phenomena such as topological states, anomalous Hall effect, quantum spin hall effect, and skyrmions [5]. However, most 2D ferromagnetic materials have Curie temperatures well below room temperature, which limits their commercial applications.

A new material, Fe_5GeTe_2 (F5GT), has recently emerged [3] with a Curie temperature as high as 332 K in bulk [6] and 280K in exfoliated thin flakes (10 nm) [3]. Unlike most other 2D ferromagnets, F5GT has magnetic easy-plane anisotropy, and the magnetization vs. temperature plots across many different studies exhibit exotic phase transitions [3-4, 6-7]. In particular, it shows a ferro- to ferri-magnetic transition at 275 K [6], suspected competition between spin and charge order at 180 K, and a transition caused by the fading of charge order at 110 K [4] (the exact transition temperatures depends on the experiment).

Our research utilizes a unique experimental technique called "magneto-thermal microscopy" [1] to study the magnetic behaviors of thin F5GT flakes (Figure 1). We can determine the in-plane local magnetic moment $\vec{M}$ of a material via the anomalous Nernst effect (ANE) by applying an out-of-plane thermal gradient $\vec{\nabla}T$, as given by the equation $\vec{E}_{ANE} = -N\vec{M} \times \vec{\nabla}T$, and measuring the anomalous Nernst voltage V_{ANE} created by the ANE electric field $\vec{E}_{ANE}$. A schematic is shown in Figure 2.

A spatially localized and short-lived thermal gradient creates an $\vec{E}_{ANE}$ that is also spatially localized and short-lived, hence the spatial resolution depends only on the size of the thermal excitation and is not inherently

limited (e.g., by diffraction). The temporal resolution depends on how long it takes the thermal gradient to equilibrize. With this, we obtain a sub-micron spatial resolution of 0.65 μm and a temporal resolution of typically < 30 ps.

Fabrication:

The F5GT nanoflake, provided by our collaborator, was placed on top of electrical contact pads fabricated via photolithography at CNF. The photomask was created with the Heidelberg Mask Writer – DWL2000, and the substrate was exposed using the GCA 6300 DSW 5X g-line Wafer Stepper. Ti/Pt was sputtered using AJA Orion Sputtering Systems to form conducting pads. The resulting wafer was diced into 5 mm × 5 mm pieces using the DISCO Dicing Saw.

To take electrical measurements (i.e., V_{ANE}), the Westbond 7400A Ultrasonic Wire Bonder was used to wirebond the contact pads to an electrical circuit component.

Conclusions and Future Steps:

While magneto-thermal microscopy has been used in the past to study various ferromagnetic and antiferromagnetic metals and insulators, this study is the first to apply it to 2D materials. Our preliminary results confirm that we can use magneto-thermal microscopy to study and image magnetization of 2D ferromagnets as shown in Figure 3. Magnetic domains are visible at an applied field of 67 G at 77 K, and we can characterize its magnetic properties by varying the field and temperature, alongside taking magnetic hysteresis measurements. With this, we would like to further investigate the exotic phase transitions at 180K and 110K, which Wu, et al. (2021) proposed is due to the competing charge and spin orders [4]. We would like to expand upon this topic by probing the magnetization vs. temperature behavior at different field cooling to help elucidate the energy barriers between the competing orders, as well as magnetic imaging to illustrate the spatial extent of the different phases. In addition, our magneto-thermal microscopy can not only measure magnetization via ANE, but it is also capable of current imaging, which can give different signatures of the charge and spin order.

References:

[1] J. M. Bartell, D. H. Ngai, Z. Leng, G. D. Fuchs, Nat. Commun., 6, 8460 (2015).

[2] C. Zhang, J. M. Bartell, J. C. Karsch, I. Gray, and G. D. Fuchs, Nano Lett., 21, 4966-4972 (2021).

[3] A. F. May, et al., ACS nano, 13, 4436-4442 (2019).

[4] X. Wu, et al., Phys. Rev. B., 104, 165101 (2021).

[5] K. S. Burch, D. Mandrus, and J.-G. Park, Nature, 563, 47-52 (2018).

[6] L. Alahmed, et al., 2D Mater. 8, 045030 (2021).

[7] H. Zhang, et al., Phys. Rev. B., 102, 064417 (2020).

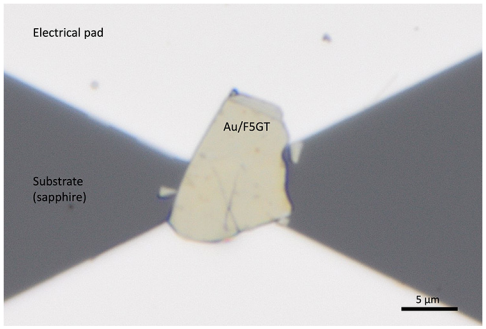

Figure 1: Optical image of a F5GT sample, Au coated to prevent degradation.

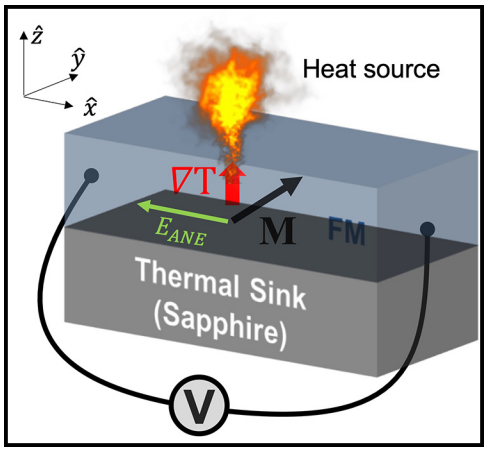

Figure 2: Schematic of the magneto-thermal microscopy technique, which exploits the anomalous Nernst effect to extract the local magnetic moment of a material.

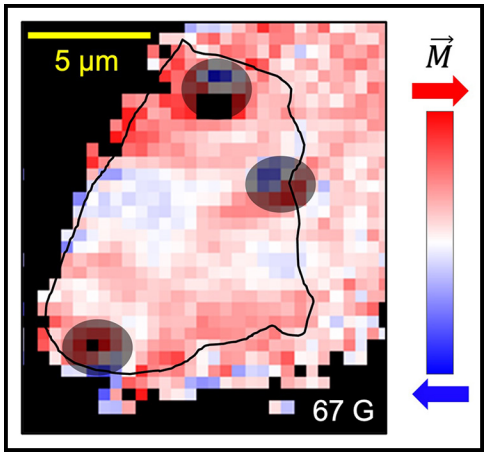

Figure 3: Magnetization image of F5GT sample shown in Figure 1 (outlined here) taken with magneto-thermal microscopy. The sample was cooled to 77 K then an external field of 67 G was applied. Magnetic domains are visible. Highly noisy parts are blacked out or shaded.

Magnetic Field Sensor Based on Spin-Hall Nano-Oscillators

CNF Project Number: 2091-11
Principal Investigator(s): Gregory D. Fuchs
User(s): Yanyou Xie

Affiliation(s): Applied and Engineering Physics, Cornell University

Primary Source(s) of Research Funding: Cornell Center for Materials Research

Contact: gdf9@cornell.edu, yx322@cornell.edu

Primary CNF Tools Used: JEOL 9500, SÜSS MA6 Contact Aligner

Abstract:

Spin-Hall nano-oscillators (SHNOs) are magnetic bilayer devices that convert DC charge current to microwave frequency magnetic oscillations under external magnetic field. The oscillation frequency of a SHNO is linearly dependent on the external magnetic field strength, and thus SHNOs can be used as bias magnetic field sensors. We demonstrate the ability of our SHNO sensor to sense small AC magnetic field with a detectivity of less than 1 $\mu T/\sqrt{Hz}$ for AC magnetic field frequency > 20-100 Hz, despite having small effective sensing area ranging from 0.32 μm² tp 0.071 μm².

Summary of Research:

The spin Hall effect (SHE) is the generation of transverse spin currents by electric currents. In a non-magnetic material (NM), this leads to the accumulation of spins with opposite polarization at opposite edges of the NM [1,2]. By placing a nonmagnetic film on top of a ferromagnetic film, the spin current generated in the NM can diffuse into the ferromagnet (FM), providing spin transfer torque (STT) to the FM [1]. Under suitable conditions, the STT is able to compensate the damping of magnetic precession, leading to steady precession of magnetization [3]. With this principle, spin-Hall nano-oscillators (SHNOs) are developed as a bilayer system consisting of NM and FM, patterned as nanowires or nanoconstrictions.

In our study we fabricated arrays of four $Ni_{81}Fe_{19}$ (5 nm)/ $Au_{0.25}Pt_{0.75}$ (5 nm) constriction-based SHNOs on 20.5 μm × 4 μm wires. Devices included both single w = 150 nm constriction and arrays of four w = 150 nm constrictions separated by a = 350 nm, with a lateral shift along -30° from the x axis, perpendicular to the magnetic field direction (Figure 1). This shifted design is to maximize the overlap between spin wave modes, as spin wave emission is perpendicular to magnetic field [4]. We used JEOL 9500 for the e-beam patterning of the SHNOs, and SÜSS MA6 contact aligner and evaporator for depositing contact pads for electrical measurements.

We use a home-built spectrum analyzer (Figure 1) to perform auto-oscillation measurements and sensing. The device is placed in an electromagnet which applies a magnetic field H = 400 Oe. A DC charge current I_{dc} is

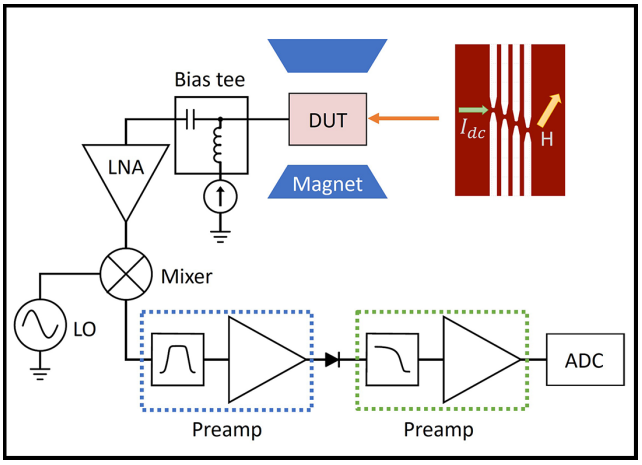

Figure 1: Schematic of measurement circuit and device under test.

applied to the device to excite auto-oscillation. The output gigahertz signal is then amplified and down-convert to megahertz (MHz) frequency by mixing it with the output from a local oscillator (LO). The output MHz signal then goes through a preamplifier before being converted to voltage signal by a RF diode. This voltage signal then goes through another preamplifier and is finally converted to a digital signal.

As we scan the frequency of LO, when the frequency of LO matches the auto-oscillation frequency from SHNO device, a peak shows up. To operate the SHNO device as a sensor, we keep the frequency of LO at the steepest slope on the peak and monitor the output voltage. As

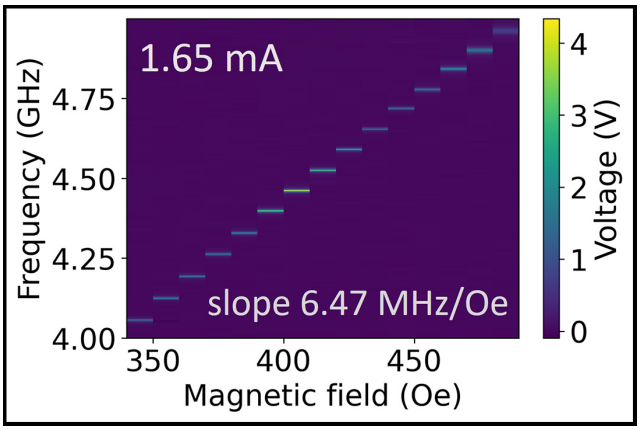

Figure 2: Auto-oscillation frequency dependence on external magnetic field under charge current I_{dc} = 1.65 mA.

the external magnetic field slightly deviates, the output voltage changes and thus we are able to measure the change in the external magnetic field.

Figure 2 shows the linear dependence of oscillation frequency on the array device under an external magnetic field at I_{dc} = 1.65 mA, with a slope df/dH = 6.47 × 10^{-3} GHz/Oe. Averaging 3000 scans over the same frequency range yields a linewidth of 6.4 MHz and a maximum dV/df = 312 V/GHz, corresponding to a sensor sensitivity $S = dV/dH$ = 2.02 V/Oe.

The detectivity of sensor is characterized by measuring the linear spectral density and dividing by the sensitivity at the optimal operating conditions. For this sensor, the detectivity goes below 1 $\mu T/\sqrt{Hz}$ for AC magnetic field frequency > 20 Hz, shown in Figure 3. The noise floor of our SHNO sensor is close to $1/\sqrt{f}$ line, indicating the noise in our sensor is dominated by the pink noise. Note that the effective sensing area is the constriction region, which is less than 0.32 μm².

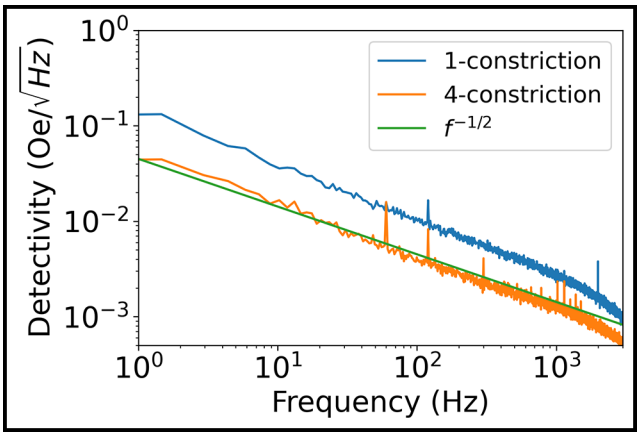

Figure 3: Noise floor of SHNO sensor at optimal operating conditions in comparison to $1/\sqrt{f}$ line.

We also fabricated a 1-constriction device with constriction width w = 150 nm for comparison. For the 1-constriction device, the detectivity goes below 1 $\mu T/\sqrt{Hz}$ for AC magnetic field frequency > 100 Hz (Figure 3), but the effective sensing area is reduced to 0.071 μm².

To demonstrate the ability to sense small magnetic variation, we place the 4-constriction array in an AC modulating field with a rms value of 0.153 Oe, and measure the output from the senor and from a Gaussmeter with its probe near the sensor. From Figure 4, the output from our sensor agrees well with the Gaussmeter.

Conclusions and Future Steps:

We developed a bias magnetic field sensor based on spin-Hall nano-oscillators to sense small variation in magnetic field within a nanoscale area, which has a detectivity of less than 1 $\mu T/\sqrt{Hz}$ for AC magnetic field frequency > 20 Hz. We have characterized quasi-DC sensing for up to kilohertz-scale frequencies. We plan to extend the measurement range up to MHz based on sideband modulation.

References:

[1] J. Sinova, et al., "Spin Hall effects," Reviews of Modern Physics, vol. 87, no. 4, p. 1213, 2015.

[2] M. D'yakonov and V. Perel, "Possibility of orienting electron spins with current," Soviet Journal of Experimental and Theoretical Physics Letters, vol. 13, p. 467, 1971.

[3] D. C. Ralph and M. D. Stiles, "Spin transfer torques," Journal of Magnetism and Magnetic Materials, vol. 320, no. 7, pp. 1190-1216, 2008.

[4] T. Kendziorczyk and T. Kuhn. "Mutual synchronization of nanoconstriction-based spin Hall nano-oscillators through evanescent and propagating spin waves," Physical Review B, vol. 93, no. 13, p.134413, 2016.

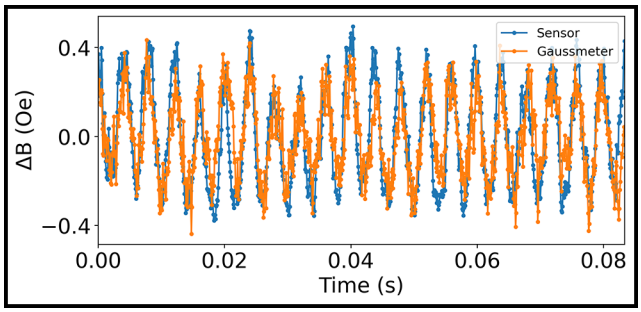

Figure 4: Comparison of measurements of a 251 Hz modulation field with a rms 0.153 Oe from the 4-constriction SHNO sensor and the Gaussmeter.

Towards Building a Bright Single-Photon Source with h-BN Defect Emitters

CNF Project Number: 2126-12

Principal Investigator(s): Gregory D. Fuchs[1]

User(s): Jialun Luo[2]

Affiliation(s): 1. Applied and Engineering Physics, 2. Department of Physics; Cornell University

Primary Source(s) of Research Funding: National Science Foundation (ECCS-1839196)

Contact: gdf9@cornell.edu, jl3562@cornell.edu
Website: http://fuchs.research.engineering.cornell.edu

Primary CNF Tools Used: AJA Sputtering System, OEM Endeavor AlN Sputtering System, JEOL 9500, JEOL 6300, PT770 Etcher, AJA Ion Mill, P-7 Profilometer, GCA 5x Stepper

Abstract:

Single-photons are essential in realizing photon-based quantum technologies [1]. Defect emitters in hexagonal boron nitride (h-BN) have been found to be bright and photostable, making them good candidates for implementing single-photon sources. We developed a fabrication process for an inverse-design cavity device from AlN for efficient photon-extraction from the defect emitters. We present an update on our work-in-progress on the fabrication and characterization of the device.

Summary of Research:

Single-photon sources are important pillars in quantum technologies such as quantum communication protocols [1,2], precision metrology [3], and quantum sensing. Building a single-photon source involves two parts: 1) a single-photon emitter and 2) a photon-extraction method. Hexagonal boron nitride (h-BN) hosts atomic defects that, upon optical excitation, emit bright and photostable fluorescence [5,6]. The zero-phonon line fluorescence from carbon-related h-BN defects falls near 585 nm [6]. Previous publications suggest that carbon ion-implantation can deterministically create these defect emitters [7]. Since h-BN is a van der Waals material that can be prepared into flakes thinner than a tenth of the fluorescence wavelengths, photons emitted from defects hosted within naturally suffer less from total internal reflection. However, the far-field radiation power from these defect emitters typically concentrates at higher angles, which means a high numerical aperture microscope objective is necessary to collect the light.

Our collaborator from the Rodriguez group then calculated a nanostructure to aid the photon collection [8]. The nanostructure shortens a dipole emitter's lifetime when one is placed at the center high field region due to the Purcell effect, and it modifies the near-field dielectric environment of the dipole emitter so that more photons are emitted into a smaller cone for lower numerical aperture lenses to collect (Figure 1).

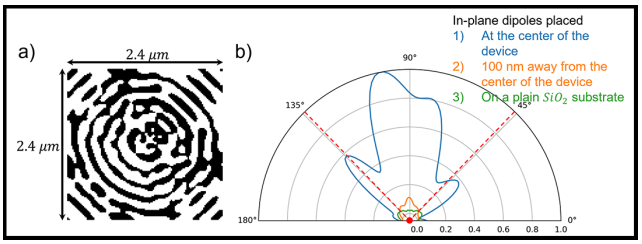

Figure 1: a) Top-down view of an optimized structure pattern for an in-plane dipole emitter. The thickness is 300 nm. b) Far-field radiation patterns comparison among dipole emitters placed at the center of the device, 100 nm shifted away from the center of the device, and placed on a plain SiO_2 substrate. The red dashline indicates the maximum collection angle of a 0.7 NA microscope objective.

In this work, we attempt to build a h-BN defect emitter-based single-photon source integrated with a nanostructure to efficiently extract the single photons.

We fabricated the current generation devices on Si wafer, which allows us to cleave the sample and inspect the cross section. The devices are made from AlN sputtered by the OEM Endeaver M1 AlN sputter system. We chose hydrogen silsesquioxane (HSQ) as our resist layer due to its 10 nm spatial resolution with electron-beam (e-beam) lithography. The nanostructure is patterned by the JEOL 9500 e-beam lithography system. The pattern is transferred to a hard mask layer made of

Ni by ion milling. Then, the devices are etched by reactive ion etch with chlorine/oxygen plasma. While reactive ion etch has high directionality, the device aspect ratio is as high as 5 to 1, so we faced the problem of angled sidewalls. We optimized the etch recipe and reached a sidewall angle of 82 degrees (Figure 2). According to the calculation, such a device can still enhance the photon collection by 7-to-10-fold.

Following the Aharonovich group result [7], we send exfoliated h-BN flakes with thicknesses ranging from tens to hundreds of nm for carbon ion-implantation process. However, the resulting flakes contain mostly short-lived emitters with broad emission spectra (Figure 3), rendering h-BN flakes not suitable for single-photon sources. We also found that the thin h-BN flakes become much harder, if not impossible, to pick up with our 2D material transfer techniques.

We tried characterizing the inverse-design cavity nanostructures by transferring a 100-nm sized h-BN flake over (Figure 4), however, the fluorescence and the collected spectra showed no enhancement, likely because the h-BN flake drastically changed the dielectric environment and broke the nanostructure design assumption that only a thin layer of h-BN is placed on it.

Future Work:

We are trying to characterize the inverse-design cavity nanostructures with commercially available CdSe quantum dots which are of 10 nm in size. The characterization result can provide guidance for the next steps.

Acknowledgements:

We would like to thank members of the Rodriguez Group on the discussion on and their designs of the inverse-design cavity nanostructures.

References:

[1] Bennett, C. H., and Brassard, G. Quantum cryptography: Public key distribution and coin tossing. Theoretical Computer Science 560, 7-11 (2014).

[2] Waks, E., Inoue, K., Santori, C., Fattal, D., Vuckovic, J., Solomon, G. S. and Y. Yamamoto, "Quantum cryptography with a photon turnstile," Nature 420, 762 (2002).

[3] Giovannetti, V. Lloyd, S. and Maccone, L., Quantum-enhanced measurements: Beating the standard quantum limits, Science 306, 1330 (2004).

[4] Thiel, C., Bastin, T., Zanthier J. von and G. S. Agarwal, Sub-Rayleigh quantum imaging using single photon soucres, J. Lightwave Technol. 20, 2154 (2002).

[5] Aharonovich, I., Englund, D., and Toth, M. Solid-state single-photon emitters. Nature Photonics 10, 631-641 (2016).

[6] Jungwirth, N. R., and Fuchs, G. D. Optical Absorption and Emission Mechanisms of Single Defects in Hexagonal Boron Nitride. Phys. Rev. Lett. 119, 057401 (2017).

[7] Mendelson, N., et al. Identifying carbon as the source of visible single-photon emission from hexagonal boron nitride. Nat. Mater. 20, 321-328 (2021).

[8] Molesky, S., et al. Inverse design in nanophotonics. Nature Photonics 12, 659-670 (2018).

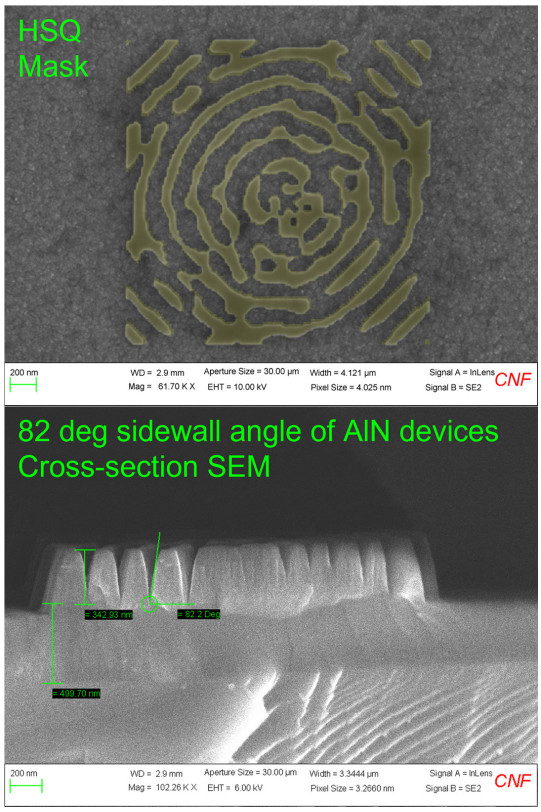

Figure 2: Upper: Developed HSQ mask overlayed with the design pattern (in yellow) Lower: The cross-section SEM of etched AlN devices showing an 82-degree sidewall angle.

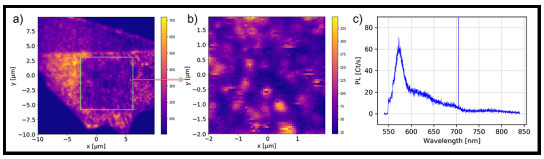

Figure 3: a) A typical fluorescence map under 532-nm laser excitation. b) A finer fluorescence map zoomed into the boxed region in a), there are point-like emitters in general. c) Typical spectrum of the point-like emitters. While the zero-phonon line centers around 585 nm, the linewidth is broad (~20 nm).

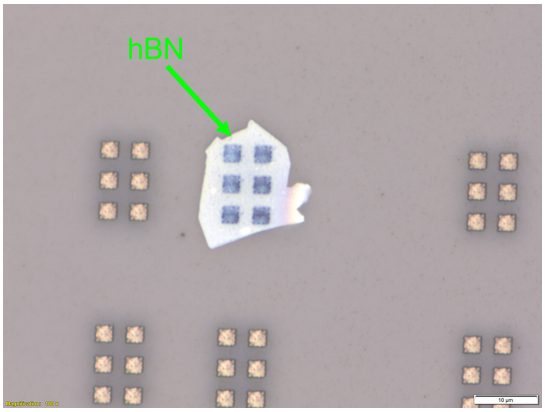

Figure 4: An optical image of a 100 nm thick h-BN flake placed over six inverse-design cavity devices.

Quantifying NV Center Spectral Diffusion by Symmetry

CNF Project Number: 2126-12

Principal Investigator(s): Gregory D. Fuchs

User(s): Brendan Andrew McCullian

Affiliation(s): School of Applied and Engineering Physics, Cornell University

Primary Source(s) of Research Funding: DARPA Driven and Nonequilibrium Quantum Systems (DRINQS) Program, Department of Energy Office of Basic Energy Sciences, Office of Naval Research

Contact: gdf9@cornell.edu, bam327@cornell.edu

Primary CNF Tools Used: GCA 6300 DSW 5X g-line Wafer Stepper, Heidelberg Mask Writer – DWL2000, AJA Sputter Deposition, Westbond 7400A Ultrasonic Wire Bonder

Abstract:

The spectrally narrow, spin-dependent optical transitions of nitrogen vacancy (NV) center defects in diamond can be harnessed for quantum networking applications. Two challenges limit scalability: defect-to-defect variations of the optical transition frequencies caused by local strain variation, and spectral diffusion of the optical frequencies on repeated measurement caused by photoexcitation of nearby charge traps. We quantify spectral diffusion and strain, decomposing each into components of specific symmetry, and investigate correlations between spectral diffusion, strain, and depth from surface. Our correlation study reveals that ideal NV centers are likely found to have large transverse strain and are at depths which balance surface charge trap effects with laser focal aberration effects.

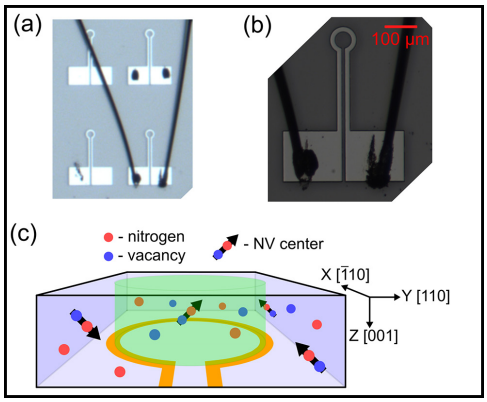

Figure 1: (a, b) Optical micrographs of litho-graphically defined loop antennas grown on diamond surface and wire bonds to microwave source. (c) Schematic of diamond sample with spatially isolated single NV centers and nearby bulk charge traps.

Summary of Research:

NV centers in diamond exhibit narrow, spin-preserving optical transitions at cryogenic temperatures that can be harnessed for quantum networking applications [1]. Such applications are limited by two key factors: spectral diffusion of the optical transition frequencies on repeated measurement [2] and defect-to-defect variation in optical transition frequencies resulting from strain [3]. Though there has been significant progress toward quantum networking with NV centers [4], only carefully chosen defects are able to be incorporated into such devices.

We quantify spectral diffusion and investigate how spectral diffusion correlates with other physical parameters of NV centers. We quantify both the spectral diffusion and the static strain for 16 individual bulk NV centers, breaking each into components of a given Jahn-Teller symmetry. We then calculate the correlation and significance (p-value) between the different components of spectral diffusion, components of strain, and depth from the diamond surface.

Our sample (Figure 1) is a type IIa diamond with individually addressable single NV centers formed via electron irradiation and subsequent annealing. We patterned a microwave loop antenna for spin control on the diamond surface, using the Heidelberg Mask Writer – DWL2000 to make the mask, the GCA 6300 DSW 5X g-line stepper to write the pattern,

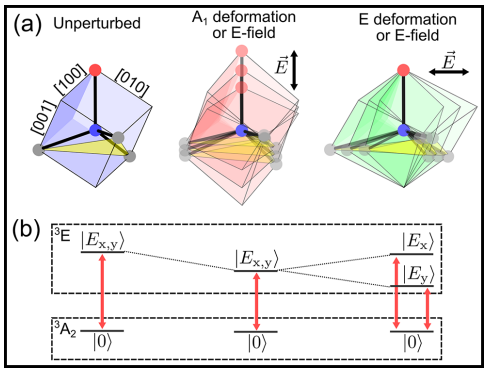

Figure 2: (a) An unperturbed NV center has C_{3v} symmetry and can undergo either A_1-symmetric (longitudinal) or E-symmetric (transverse) perturbation from strain or electric field. (b) Longitudinal perturbations globally shift the optical transition frequencies, while transverse perturbations split the excited-state orbital doublet into two branches.

the AJA sputter deposition system to deposit 25 nm of Ti and 225 nm of Pt. After lift-off the device was wire bonded to our cryostat microwave feed lines using the Westbond 7400A Ultrasonic Wire Bonder.

We perform photoluminescence excitation (PLE) spectroscopy measurements by tuning a red laser (~637.2nm) across the resonant optical transitions of the NV center while counting photons emitted into the phonon sideband. The spin-preserving optical transitions are from orbital singlet, spin triplet ground states to orbital doublet, spin triplet excited states. All measurements are carried out in a helium flow cryostat at 10 K.

An unperturbed NV center has C_{3v} point-group symmetry and two degenerate spin-0 optical transition energies (Figure 2) [5]. Longitudinal (A_1) perturbations shift the excited states together, while transverse perturbations (E) split the orbital branches.

We characterize the strain components for each NV center by applying 637.2 nm and 532 nm laser pulses while tuning the red laser frequency. The 532 nm laser ensures that the defects is always in spin-0. As shown in Figure 3, by measuring the splitting of the two optical transitions, the rotation of the optical dipole [6], and the absolute center frequency of the PLE peaks we fully quantify the strain components for each NV center.

We then characterize the spectral diffusion. We apply a single green laser pulse followed by a full red laser sweep and repeat 125 times on each defect. These spectra are summed, and the changes in splitting and center frequency are recorded for each of the sweeps in a histogram. By extracting the width of these histograms via fitting with a Gaussian response we can quantify the longitudinal and transverse components of spectral diffusion.

We calculate the correlations and p-values of each component of spectral diffusion, static strain, as well as the measured depth from surface. These correlations reveal that both strain and spectral diffusion are dominated by longitudinal perturbations. Also, NV centers with larger transverse strain are more protected from orthogonal and transverse spectral diffusion. Last, for bulk NV centers the spectral diffusion increases with depth due to laser aberration.

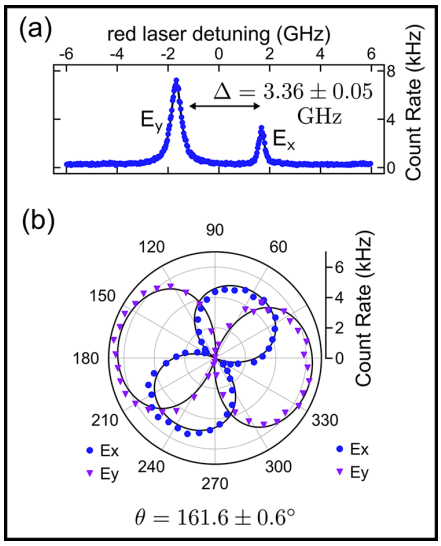

Figure 3: (a) PLE frequency sweep and extracted strain splitting Δ from two Lorentzian fits. (b) PLE laser polarization rotation and extracted dipole rotation θ.

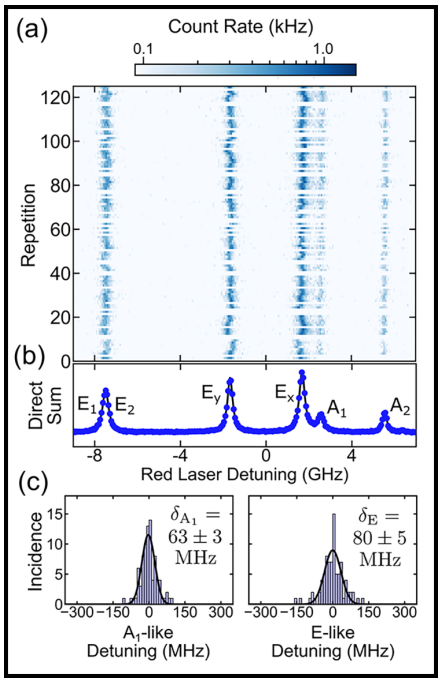

Figure 4: (a) 125 repetitions of frequency-swept PLE showing spectral diffusion on repeated measurement. (b) Direct sum of repeated PLE response. (c) Histogram of longitudinal and transverse spectral diffusion components including Gaussian fits to quantify degree of each symmetry of spectral diffusion.

Conclusions and Future Steps:

Our results indicate that NV centers with large transverse strain will on average have reduced spectral diffusion. This can provide a quick means of searching for good candidate defects for quantum networking. Also, defects should be located at a depth which balances the spectral diffusion known to occur from near-surface charge traps [7] with the depth-related spectral diffusion we uncovered. Future work will investigate how NV centers driven with mechanical resonators can be made robust to spectral diffusion.

Our manuscript is under review, and a preprint is available on arXiv [8].

References:

[1] L. Childress, et al., Phys. Rev. A 72, 052330 (2005).
[2] K. M. C. Fu, et al., Phys. Rev. Lett. 103, 256404 (2009).
[3] F. Grazioso, et al., App. Phys. Lett. 103, 101905 (2013).
[4] S. L. N. Hermans, et al., Nature 605, 663 (2022).
[5] J. R. Maze, et al., New J. Phys. 13, 025025 (2011).
[6] K. W. Lee, et al., Phys. Rev. Appl. 6, 034005 (2011).
[7] M. Ruf, et al., Nano Lett. 19, 3987 (2019).
[8] B. A. McCullian, et al., arXiv:2206.11362 (2022).

Building van der Waals Pi Josephson Junctions

CNF Project Number: 2633-18

Principal Investigator(s): Jie Shan, Kin Fai Mak

User(s): Kaifei Kang

Affiliation(s): Laboratory of Atomic and Solid State Physics,
School of Applied and Engineering Physics; Cornell University

Primary Source(s) of Research Funding: United States Army Research Office

Contact: jie.shan@cornell.edu, kinfai.mak@cornell.edu, kk726@cornell.edu

Primary CNF Tools Used: Autostep i-line Stepper, Hamatech Wafer Processor Develop,
Heidelberg Mask Writer - DWL2000, Photolithography Spinners,
SC4500 Odd/Even-Hour Evaporator, DISCO Dicing Saw

Abstract:

At the interfaces of superconductors (SC) and ferromagnets (FM), exotic Cooper pairs with finite center-of-mass momentum can be realized [1]. Here we build van der Waals ferromagnetic Josephson junctions using atomically thin $NbSe_2$ and $Cr_2Ge_2Te_6$ (CGT) flakes. We observe a damped-oscillatory dependence of the Josephson critical current density on the CGT barrier thickness, which is the definitive evidence for a thickness-driven 0 to π transition. Near the transition, we observe 0 – π Josephson junctions with zero critical current at zero magnetic field. Our work demonstrates the thickness-driven 0 to π transition in van der Waals Josephson junctions and 0 – π Josephson junctions with uniform barrier thickness.

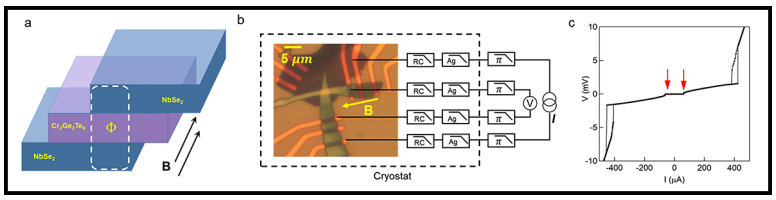

Figure 1: $NbSe_2/Cr_2Ge_2Te_6/NbSe_2$ Josephson Junctions. a, Schematics of the device structure. The magnetic field is applied to the in-plane direction, which produces a magnetic flux through the cross-sectional area of the device (marked by the white dashed rectangle). b, Schematics for the electrical measurements. All electrical lines are filtered by π, silver-epoxy, and low-temperature RC filters. c, I-V *characteristic of a device with a CGT barrier thickness of about 3.6 nm.*

Summary of Research:

The recent discovery of two-dimensional (2D) layered superconducting and magnetic materials provides a new platform to realize π Josephson junctions (JJs) with atomically uniform thickness and sharp interfaces via van der Waals stacking [2,3]. In this project, we fabricate JJs using van der Waals superconductor $NbSe_2$ and semiconducting ferromagnet $Cr_2Ge_2Te_2$ (CGT) (Figure 1a).

Figure 1b shows the schematics for the electrical measurements. The JJs are current-biased, and the voltage drop across the JJs is measured. Radiation with frequencies above 30 kHz is filtered to avoid unwanted quasiparticle excitations. Figure 1c shows the current-voltage characterization of a JJ with a 3.6-nm CGT barrier. The voltage drop V across the JJ vanishes when the bias current I is smaller than the Josephson critical current of $I_c \approx 63$ μA (marked by the red arrows). At a large bias current of $I \sim 500$ μA, a second voltage jump of about 3 mV is observed, corresponding to the superconducting critical current of the $NbSe_2$ flakes.

We study the thickness dependence of the Josephson critical voltage $V_c = I_c R_n$. Here R_n is the resistance of the JJs when $I > I_c$. Figure 2 shows V_c as a function of the CGT thickness, d. As d increases, V_c first decreases for $d <$ 8.4 nm, increases for 8.4 nm $< d <$ 9.9 nm, and then vanishes when $d \approx 12.3$ nm. Such a thickness dependence of V_c is consistent with the thickness-driven 0 to π transition with a critical barrier thickness of $d_c = 8.4$ nm.

We also examine the magnetic interference patterns in JJs with different barrier thicknesses. Figures 3a-3d show the sample differential resistance as a function of magnetic field (B) and bias current in JJs with selected CGT barrier thickness of 5.2, 7.7, 9.1, and 9.9 nm. For JJs with CGT thicknesses away from the critical thickness (Figure 3a and Figure 3d), regular Fraunhofer patterns are observed with pronounced central lobes near B = 0 T. However, for JJs with CGT barrier with just one layer thinner (Figure 3b) or one layer thicker (Figure 3c) than the critical thickness d_c, we observe zero critical current near B = 0 T, which signifies the formation of 0 – π JJs. The observation of the 0 – π JJs with uniform barrier thickness is attributed to the inhomogeneous magnetization induced by the magnetic domain walls in CGT, which is reported by a recent Lorentz TEM study [4].

In conclusion, we have fabricated high-quality van der Waals ferromagnetic Josephson junctions. By varying the thickness of the ferromagnetic barrier, we observe a damped oscillatory behavior for the JJ critical current density and thus a thickness-driven 0 to π transition. Near the transition, we identify 0 – π JJs with zero critical current near zero magnetic field and uniform barrier thickness.

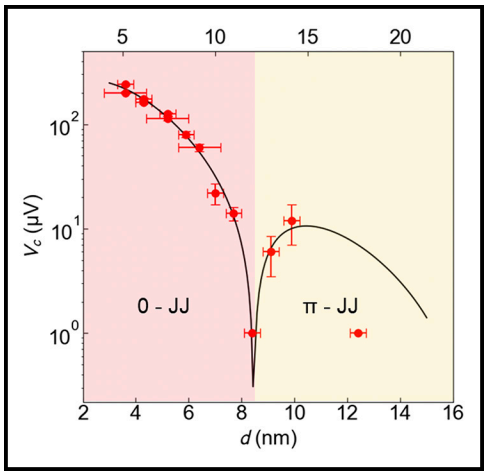

Figure 2: Thickness-driven 0 to π transition. Critical voltage V_c as a function of CGT barrier thickness. JJs have zero phase difference in red dashed region and π phase difference in the orange region.

References:

[1] Buzdin, A. I. Proximity effects in superconductor-ferromagnet heterostructures. Rev. Mod. Phys.77, 935 (2005).

[2] Saito, Y. et al. Superconductivity protected by spin-valley locking in ion-gated MoS_2. Nat. Phys. 12, 144-149 (2016).

[3] Mak, K. F., Shan, J. and Ralph, D. C., Probing and controlling magnetic states in 2D layered magnetic materials. Nat. Rev. Phys.1, 646-661 (2019).

[4] Idzuchi, H. et al., Unconventional supercurrent phase in Ising superconductor JJ with atomically thin magnetic insulator. Nat. Comm.12, 5332 (2021).

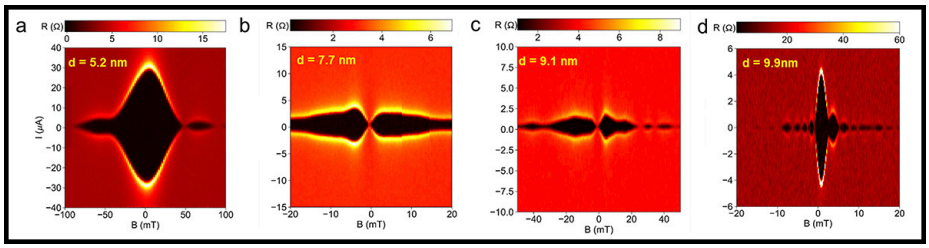

Figure 3: Magnetic interference pattern of the Josephson supercurrent. a – d, Magnetic interference pattern of the supercurrent in JJs with barrier thickness of 5.2 nm (a), 7.7 nm (b), 9.1 nm (c), and 9.9 nm (d). The magnetic field is scanned in the forward direction.

Strongly Correlated Excitonic Insulator in Atomic Double Layers

CNF Project Number: 2633-18

Principal Investigator(s): Jie Shan, Kin Fai Mak

User(s): Liguo Ma, Phuong X. Nguyen

Affiliation(s): Laboratory of Atomic and Solid State Physics,
School of Applied and Engineering Physics; Cornell University

Primary Source(s) of Research Funding: The US Department of Energy (DOE)

Contact: jie.shan@cornell.edu, kinfai.mak@cornell.edu, lm837@cornell.edu, pxn2@cornell.edu

Primary CNF Tools Used: Autostep i-line Stepper, Hamatech Wafer Processor Develop, Heidelberg Mask Writer - DWL2000, Photolithography Spinners, SC4500 Odd/Even-Hour Evaporator, DISCO Dicing Saw, Zeiss Supra SEM, Nabity Nanometer Pattern Generator System (NPGS)

Abstract:

Excitonic insulators (EIs) arise from the formation of bound electron-hole pairs (excitons) in semiconductors and provide a solid-state platform for quantum many-boson physics. Here, we demonstrate a strongly correlated two-dimensional (2D) EI ground state formed in transition metal dichalcogenide (TMD) semiconductor double layers, where spatially indirect excitons form. We construct an exciton phase diagram that reveals both the exciton Mott transition and interaction-stabilized quasi-condensation through a quantum capacitance measurement.

Summary of Research:

In bulk materials, excitonic insulators (EIs) can occur in small band gap semiconductors and small band overlap semimetals [1]. In the semiconductor limit, EIs occur when the electron-hole binding energy of an exciton exceeds the charge band gap. The ground state exciton population is determined by balancing the negative exciton formation energy against the mean exciton-exciton repulsion energy.

Although the concept has been understood for a long time, establishing distinct experimental signatures of the EIs has remained challenging.

In this experiment, we employ the atomic double layer structure to establish electrical control of the chemical potential of interlayer excitons (by making separate electrical contacts to isolated electron and hole layers). Since the electron and hole wavefunctions do not interfere, macroscopic phase coherence is spontaneous, allowing exciton superfluidity.

The dipolar nature of the interlayer excitons and the reduced dielectric screening in our devices also favor strong exciton-exciton repulsion.

Figure 1 shows the device schematics and optical image of a typical device. The device is made of a $WSe_2/MoSe_2$ bilayer separated by a thin hexagonal boron nitride (h-BN) spacer. It is also encapsulated by two gates made of h-BN and graphite. Atomically thin samples of WSe_2, $MoSe_2$, h-BN and graphite were first exfoliated from their bulk crystals onto silicon substrates. Selected thin flakes of appropriate thickness and geometry were picked up one-by-one by a stamp consisting of a thin layer of polycarbonate on polydimethylsiloxane (PDMS). The complete heterostructure was then deposited onto the substrates with pre-patterned Pt electrodes.

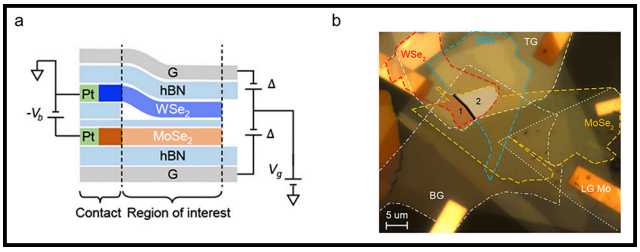

Figure 1: a, Device schematics. b, Optical microscope image of a dual-gated device. Scale bar is 5 μm.

Figure 2 (top row) shows schematics of the penetration (a) and interlayer (b) capacitance measurements. A commercial high electron mobility transistor is used

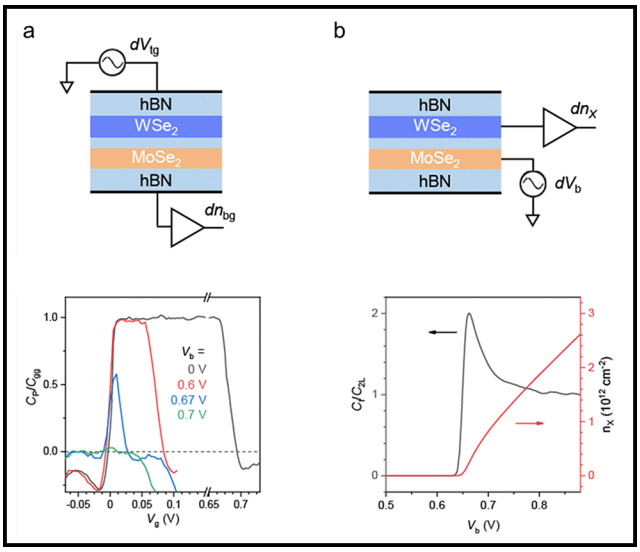

Figure 2: a, Normalized penetration capacitance as a function of gate voltage for representative bias voltages. b, Normalized interlayer capacitance (left axis) and exciton density extracted from the interlayer capacitance (right axis) as a function of bias voltage. Top row shows the schematics of the corresponding capacitance measurements.

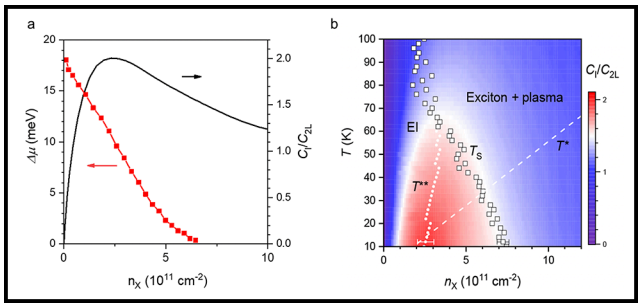

Figure 3: a, Charge gap and exciton compressibility as a function of exciton density at 15 K. b, Exciton compressibility as a function of temperature and exciton density.

as the first-stage amplifier to effectively reduce the parasitic capacitance from cabling [2]. To obtain the penetration capacitance, we apply an AC voltage (5 mV in amplitude) to the top gate and collected the signal from the bottom gate. For the interlayer capacitance, we apply an AC voltage (5 mV in amplitude) to the $MoSe_2$ layer and collected the signal from the WSe_2 layer. The measured penetration capacitance signal (Figure 2a) tracks changes in the charge gap when a bias is applied between WSe_2 and $MoSe_2$. The interlayer capacitance signal directly measures the formation of electron-hole pairs, or exciton compressibility, from which the exciton density can be obtained by integration with respect to bias voltage (Figure 2b).

We obtained exciton phase diagram in Figure 3 by combining the two measurements. The charge gap under various electron-hole pair density is measured by penetration capacitance (Figure 3a). Nonzero gap at finite density indicates that the electron-hole pairs are in the EI phase. With increasing density, the charge gap decreases to zero gradually at a critical density (the Mott density), at which the excitons are dissociated into electron-hole plasma [3]. Figure 3b shows the constructed exciton phase diagram from the measured exciton compressibility as a function of temperature and density.

The density dependence of the exciton compressibility in Figure 3 indicates the importance of exciton-exciton interactions. We consider an interacting Bose gas model [4] below the exciton ionization temperature T_s. The effective interaction strength extracted from our result is an order of magnitude larger than in other systems such as cold atoms and helium. The strong correlation is expected to suppress exciton density fluctuations [5] and enhance the effective degeneracy temperature from the degeneracy temperature T^* for non-interacting bosons to T^{**}. The region bound by T^{**} and T_s represents a degenerate exciton fluid with suppressed density fluctuations (i.e., a quasi-condensate). The strong correlation is also expected to suppress phase fluctuations and enhance the exciton superfluid transition temperature.

Our experiment paves the path for realizing the exotic quantum phases of excitons, as well as multi-terminal exciton circuitry for applications.

References:

[1] Jérome, D., Rice, T.M., and Kohn, W. Excitonic Insulator. Physical Review 158, 462-475 (1967).

[2] Ashoori, R. C., et al. Sigle-Electron Capacitance Spectroscopy of Discrete Quantum Levels. Phys. Rev. Lett. 68, 3088-3091 (1992).

[3] Mott, N.F. The transition to the metallic state. The Philosophical Magazine: A Journal of Theoretical Experimental and Applied Physics 6, 287-309 (1961).

[4] Wu, F.-C., Xue, F., and MacDonald, A.H. Theory of two-dimensional spatially indirect equilibrium exciton condensates. Physical Review B 92, 165121 (2015).

[5] Kagan, Y., Kashurnikov, V.A., Krasavin, A.V., Prokof'ev, N.V., and Svistunov, B.V. Quasicondensation in a two-dimensional interacting Bose gas. Physical Review A 61, 043608 (2000).

Superconducting Thin Film Growth, Process Development, Defects Investigation, and Device Fabrication for Radio-Frequency Accelerating Cavities

CNF Project Number: 2779-19

Principal Investigator(s): Matthias Liepe

User(s): Zeming Sun

Affiliation(s): Cornell Laboratory for Accelerator-based Sciences and Education, Cornell University

Primary Source(s) of Research Funding: the U.S. National Science Foundation under Award PHY-1549132, the Center for Bright Beams

Contact: mul2@cornell.edu, zs253@cornell.edu
Website: https://physics.cornell.edu/matthias-liepe

Primary CNF Tools Used: Thermal / E-Gun Evaporation System, Oxford FlexAL Atomic Layer Deposition System, Jelight 144AX UV Ozone Generator, Arradiance Gemstar-6 Atomic Layer Deposition System, Chemical Vapor Deposition System, Woollam Spectroscopic Ellipsometer, Zygo Optical Profilometer, P10 Profilometer

Abstract:

Superconducting radio-frequency (SRF) cavities are the key component for particle accelerators that have broad applications such as synchrotron X-ray, high-energy colliders, and extreme-UV lithography. Our research is to search for the next-generation SRF materials and surfaces beyond the industry-standard niobium (Nb). Niobium-tin (Nb_3Sn), niobium-zirconium (NbZr), Nb with a processed/designed surface, niobium titanium nitride (NbTiN), and vanadium silicate (V_3Si) are of our interest. By using facilities at the CNF, we mainly focus on SRF thin film growth, sample preparation for material characterization, post treatment to improve RF properties, and device fabrication to fundamentally understand the SRF physics. We highlight our recent success on a NbZr alloyed cavity, which is the first experimental demonstration for such cavities and shows better RF performance than a reference Nb cavity [1-3].

Summary of Research:

(1) We demonstrated a high-performance NbZr alloyed SRF cavity [1-3]. In the sample-scale study, we deposited the initial Zr films using the e-beam evaporator at CNF, and achieved different Zr surface profiles after thermal annealing. Figure 1 shows the surface morphology of the annealed samples. We found the critical temperature of these samples are improved due to the NbZr alloying. We further developed an electrochemical deposition process to scale up the alloying process to a Cornell sample test cavity, and we observed the reduction of surface resistance owing to the increased critical temperature of NbZr alloys.

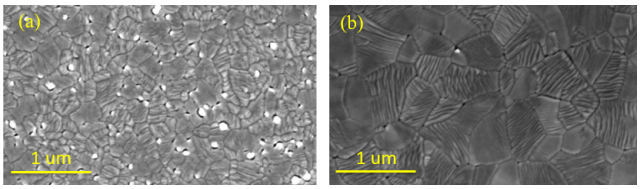

Figure 1: Surface morphology of the annealed NbZr samples with different initial Zr film thicknesses: (a) 40 nm and (b) 20 nm.

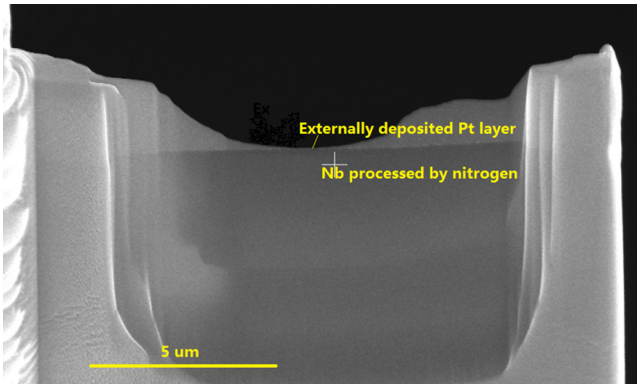

Figure 2: Cross-sectional image of a nitrogen-doped Nb specimen coated with the Pt protective layer used for scanning transmission electron microscopy.

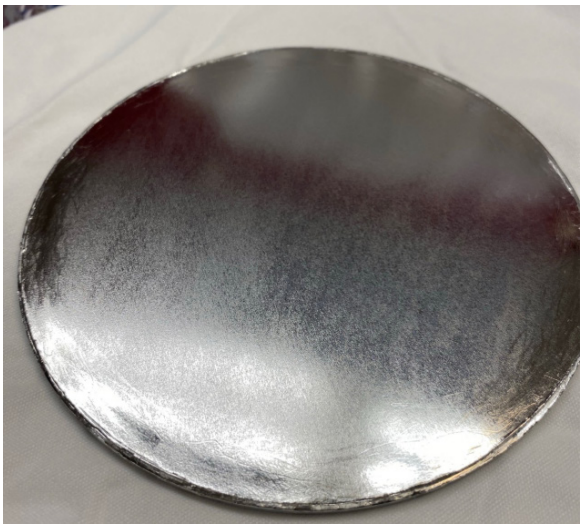

Figure 3: Picture of a Cornell sample test SRF cavity (the testing plate) with the artificially controlled surface.

(2) We demonstrated electrochemically-made Nb_3Sn thin films with extremely low surface roughness and an improved stoichiometry. Zhaslan Baraissov and Prof. David Muller's research group at Cornell Applied Physics are working on atomic analysis of these high quality Nb_3Sn films together with Nb samples processed under different treatments. To overcome the sample preparation issues before atomic imaging, we deposited an external Pt layer, at CNF, to protect the sample surface which is the most critical region for SRF applications (Figure 2).

(3) We fabricated SRF devices using the e-beam evaporator and Oxford FlexAL atomic layer deposition system at CNF to fundamentally understand the RF surface design. This year, we scaled up the artificial control process of a Nb surface to the Cornell sample test cavity. Preliminary results showed positive RF results owing to our rational surface design.

References:

[1] Z. Sun, et al., "Materials investigation and surface design of superconducting radio-frequency accelerating cavities at Cornell University", presented at the 2022 MRS Spring Meeting, Honolulu, HI, May 2022.

[2] N. S. Sitaraman, "Theory results on novel surface preparations for superconducting radio-frequency cavities", presented at the 2022 MRS Spring Meeting, Honolulu, HI, May 2022.

[3] Z. Sun, et al., "First demonstration of a ZrNb alloyed surface for superconducting radio-frequency cavities", presented at the North American Particle Accelerator Conference (NAPAC'22), Albuquerque, NM, August 2022.

Development of Fabrication Process on Strainable Polyimide Substrate

CNF Project Number: 2790-19

Principal Investigator(s): Katja Nowack

User(s): Ruiheng (Rex) Bai

Affiliation(s): Lab of Atomic of Solid State Physics, Cornell University

Primary Source(s) of Research Funding: National Science Foundation

Contact: katja.nowack@cornell.edu, rb873@cornell.edu
Website: https://nowack.lassp.cornell.edu/

Primary CNF Tools Used: Heidelberg Mask Writer - DWL2000, GCA 6300 DSW 5X g-line Wafer Stepper, Nabity System for Supra SEM, SC4500 Evaporator, Trion Etcher

Abstract:

In this project, we make bilayer graphene devices with a metal gate and electrical contacts on strainable polyimide substrates. We developed a procedure for doing photolithography with the resolution of 2.5 μm on polyimide substrate and using electron beam lithography along with etcher to pattern devices. Currently, we have achieved about 1% of strain on a graphene device and over 1% of strain on bare chip.

Summary of Research:

Theoretical calculation has shown that net orbital magnetization would appear in uniaxially strained bilayer graphene with broken inversion symmetry and current bias [1]. Similar magnetization has been observed in exfoliated single layer MoS_2 device [2].

To induce orbital magnetization in bilayer graphene, the device has to be dual gated, strained, and have electrical contact. We chose strainable polyimide substrate and used photolithography to pattern the prepattern, which includes a bottom gate, metal contacts to the device and a meander strain gauge. A picture of the prepattern is shown in the figure section. Then we transfer a boron nitride (BN) flake to the prepattern and pattern the flake so that it covers the bottom gate with electron beam (e-beam) lithography and reactive ion etching (RIE). Lastly, we transfer the rest of the stack on the chip with the conventional dry transfer technique. The polyimide substrate is soft and often has a curvature, making lithography difficult. It also has a non-negligible thermal expansion rate, making baking resist tricky.

By using nLOF negative tone photo resist, instead of bilayer photo resist, we managed to reduce the effect of substrate curvature on uniformity of resist thickness. Then we experimented with both a contact aligner and a stepper and found that a stepper gives better resolution. The substrate curvature making it hard for the mask to have uniform contact with the substrate. By the end, we were able to achieve 2.5 μm resolution with over 90% yield rate.

The difficulty we encountered when doing e-beam lithography is mostly related to baking resist (PMMA 495 A4 495). Since the substrate expand and shrink as temperature changes, the BN flake on it often gets wrinkles after baking, resulting in defective devices. We figured that by baking at a lower temperature (90°C) with longer time (20 min), we managed to reach our resolution requirements without making the BN flake wrinkle.

With the improved fabrication process, we have made several single gated devices. They could be strained to 0.5-0.7%, confirmed with Raman spectroscopy. We could induce an even larger strain on the substrate (over 1%) but could not transfer this strain onto the device. The strain on substrate is confirmed by both optical image and resistance measurements of the strain gauge.

Conclusions and Future Steps:

As we have successfully strained single gated bilayer graphene device, our next step would be to fabricate dual gated devices, which has an extra layer of graphite on top of the stack compared to our current stack. We also plan to try to increase clamping force on our device. Our current devices start to lose strain at 0.5-0.7% and we hope to increase the maximum strain we can induce on the device. One possible improvement we plan to try is to evaporate a layer of metal on the contact region on top of the device, thus clamping the device from both top and bottom.

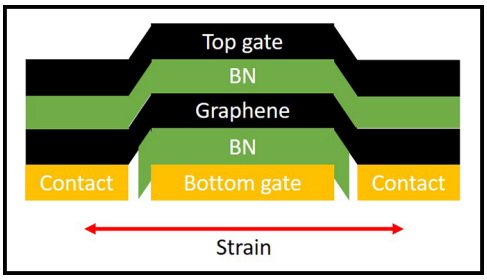

Figure 1: Cartoon picture of the structure of our final device. The red double headed arrow indicated the orientation of strain. We rely on the adhesion between the metal contact and graphene to transfer the strain from substrate to graphene. Currently, we have fabricated and strained several devices without the top graphite gate layer.

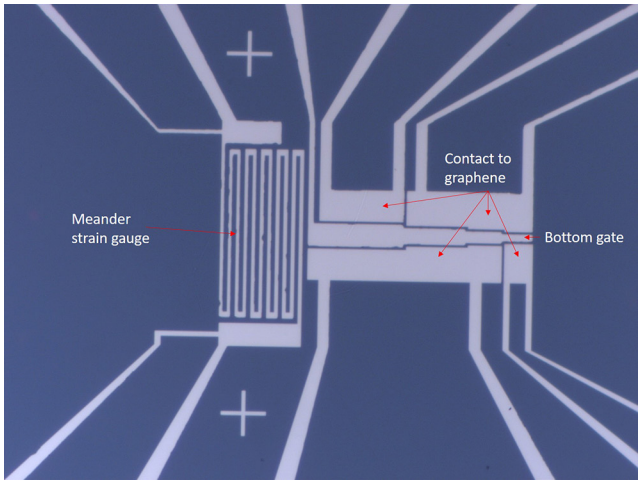

Figure 2: Prepattern that was made with photolithography and metal evaporation.

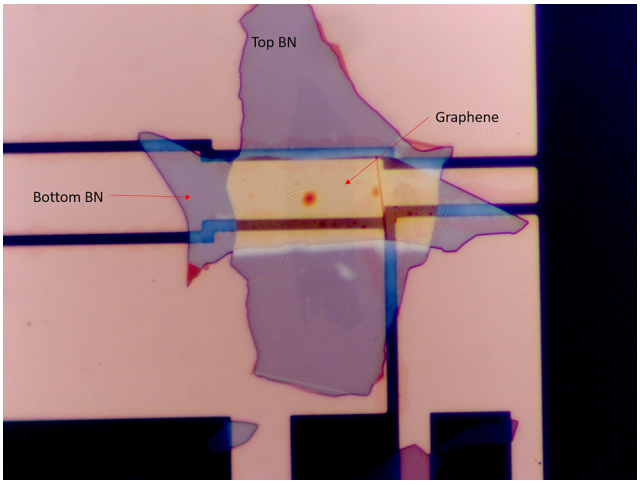

Figure 3: Fabricated device. This device does not go through the e-beam pattern step because the BN flake has the same width as the bottom, not requiring any patterning.

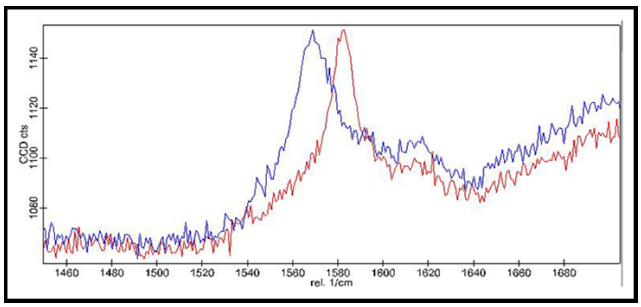

Figure 4: Raman spectrum of the device in Figure 3. The red spectrum was taken when the substrate was not strained and the blue spectrum was taken when the substrate was strained. The shift of the peak in the spectrum indicate that we have achieved ~0.7% of strain on graphene.

References:

[1] B. Schaefer, Phys. Rev. B. 103, 224426 (2021)

[2] Lee, J., Wang, Z., Xie, H., et al. Valley magnetoelectricity in single-layer MoS2. Nature Mater 16, 887-891 (2017).

Development of Engineered Gas Diffusion Layers Via Two-Photon Polymerization

CNF Project Number: 2924-21

Principal Investigator(s): Sadaf Sobhani

User(s): Giancarlo D'Orazio

Affiliation(s): Department of Mechanical and Aerospace Engineering, Cornell University

Primary Source(s) of Research Funding: Cornell University Lab Startup Grant

Contact: sobhani@cornell.edu, gd373@cornell.edu
Website: www.sobhanilab.com

Primary CNF Tools Used: NanoScribe Photonic Professional GT2

Abstract:

The need for low carbon and carbon-neutral energy sources has become increasingly clear as CO_2 emissions have continued to increase at an impressive rate. Efforts to sequester carbon show some promise, though storage remains a major issue. Utilizing this captured CO_2 in electrochemical reduction reactors can yield valuable products, such as ethanol, propanol, formic and acetic acids, among others.

As these reactors generate these products, however, the gas diffusion layer (GDL) separating the carbon dioxide gas from the cell's electrolyte begins to wet and subsequently flood with the change in product concentration; this flooding behavior severely limits operational lifespan and cell efficiency. In this work, micro-scale additive manufacturing via two-photon polymerization enables the printing of microfluidic devices. These devices were dynamically tested for flow properties via in operando testing and analysis by means of high energy X-ray imaging. The impact of architected geometry with variable surface texturing is explored, as well as the effects of electrolyte composition and surface coatings. The results of this analysis are further used in computational fluid dynamic models to better optimize GDL design to minimize flooding in subsequent designs.

Summary of Research:

In order to manufacture gas diffusion layers, the NanoScribe Photonic Professional GT2 two-photon polymerization printer was used. The high-resolution (< 1 µm voxel size) enabled by this machine allows printed porous structures with pore sizes similar to those of conventional GDLs [1,2]. The GDL designs were comprised of triply periodic minimal surfaces, a type of cubic, repeating lattice structure which is entirely formula driven. nTopology 3D modelling software was used to generate slices of these complex lattices and subsequently assembled in NanoScribe DeScribe slicing software to create a single piece while minimizing processing overhead in DeScribe.

Additively manufactured substrates were designed to serve as an interface between the printed samples and microfluidic fittings to connect the experimental setup to a micropump. These substrates were printed via stereolithography (SLA) in a resin compatible with that used by the NanoScribe GT2 to ensure bonding between printed samples and substrate. Substrates were polished to 3 µm surface finish, enabling consistent results with manual interface finding in NanoWrite.

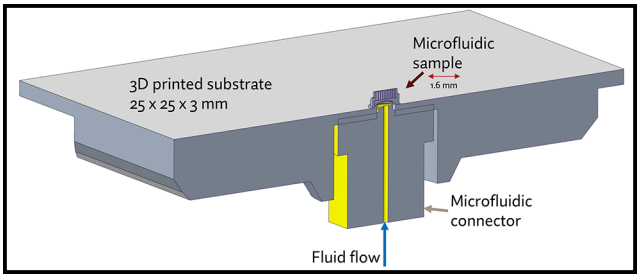

Figure 1: Section view of the microfluidic sample as mounted on the additively manufactured substrate.

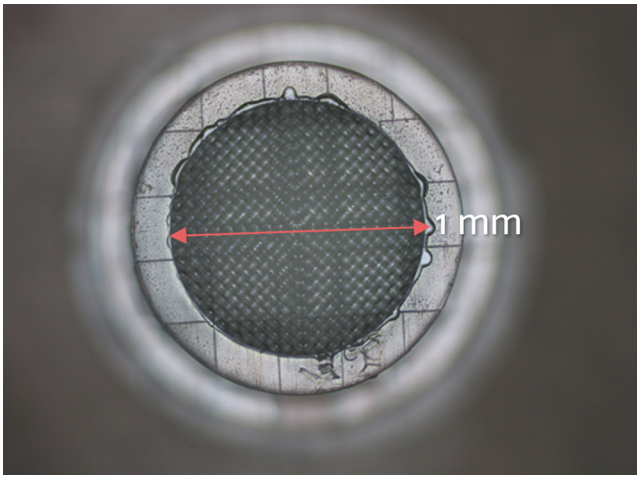

Figure 2: Top view of an as-printed sample. The internal GDL section is 1 mm in diameter with a support structure that is 1.6 mm in diameter.

Engineered GDL samples were printed in two parts on the NanoScribe GT2. First, a lower quality base layer was printed to form a support structure for the gas diffusion layer. This layer used the 25X Medium Feature Swift Mode to decrease printing time. Once this support structure was printed, the GDL was printed with the 25X objective Medium Feature Solid Mode for maximum part strength and resolution. The substrate pore directly below the samples, seen in Figure 1, enabled short development times in propylene glycol monomethyl ether acetate (PGMEA) by enhancing transport of uncured resin from the structure. Samples were developed for 30 to 60 minutes in PGMEA then 15 to 30 minutes in isopropyl alcohol (IPA). Prior work with samples printed flush to the substrate required in excess of 36 hours of development time in PGMEA and 12 hours in IPA. A finished sample, shown in Figure 2, is illustrative of the type of lattice structures developed for this experiment. After air drying, half of the samples were sent for perfluoroalkoxy alkane (PFA) coating, with the remainder uncoated for comparison purposes.

Samples were tested at Argonne National Lab's Advanced Photon Source using the 2-BM beamline. A 2 mm by 1 mm field of view was maintained while capturing at 400 frames per second in order to capture dynamic fluid flow throughout the structure. Samples were tested with pressure-driven water flow to determine flooding behavior. Pressure was ramped from 0 to 200 mBar in most cases, resulting in flow rates of approximately 2 µL/min. After data capture, XCT data was reconstructed with Tomopy and Tomocupy [3,4]. The pressure and flow rate were compared to the flooding behavior of each design.

Preliminary results validate the expected effect of the hydrophobic coating, with significantly decreased flooding compared to uncoated samples. Figure 3 demonstrates the clear difference in flooding behavior in coated versus uncoated samples, validating the coating process.

Further work is ongoing to determine the impact of lattice morphology on GDL flooding.

References:

[1] D. Corral, et al., "Advanced manufacturing for electrosynthesis of fuels and chemicals from CO_2," Energy Environ. Sci., vol. 14, no. 5, pp. 3064-3074, May 2021, doi: 10.1039/D0EE03679J.

[2] Y.-R. Lin, et al., "Vapor-Fed Electrolyzers for Carbon Dioxide Reduction Using Tandem Electrocatalysts: Cuprous Oxide Coupled with Nickel-Coordinated Nitrogen-Doped Carbon," Advanced Functional Materials, vol. 32, no. 28, May 2022, doi: 10.1002/adfm.202113252.

[3] D. Paganin, S. C. Mayo, T. E. Gureyev, P. R. Miller, and S. W. Wilkins, "Simultaneous phase and amplitude extraction from a single defocused image of a homogeneous object," J Microsc, vol. 206, no. Pt 1, pp. 33-40, Apr. 2002, doi: 10.1046/j.1365-2818.2002.01010.x.

[4] D. Gürsoy, F. De Carlo, X. Xiao, and C. Jacobsen, "TomoPy: a framework for the analysis of synchrotron tomographic data," J Synchrotron Radiat, vol. 21, no. Pt 5, pp. 1188-1193, Aug. 2014, doi: 10.1107/S1600577514013939.

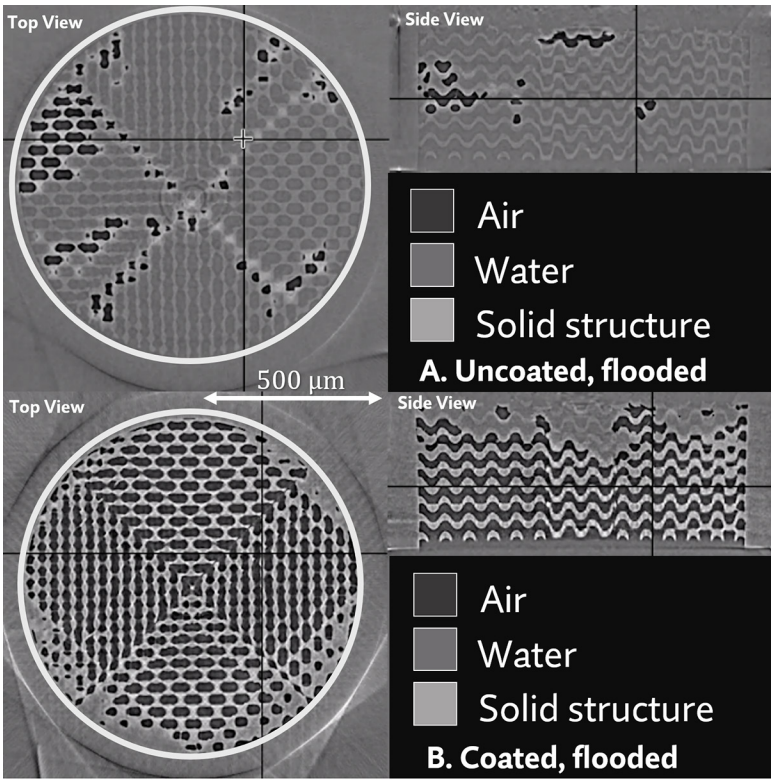

Figure 3: Real-time XCT reconstruction of an uncoated sample (top) and a PFA coated sample (bottom) during in operando *testing with water. Flooding is significant in the uncoated sample.*

Design of Porous Substrates for Enhanced Development of Microfluidic Devices

CNF Project Number: CNF Fellowship

Principal Investigator(s): Christopher Kemper Ober[1]

User (s): Giancarlo D'Orazio[2]

Affiliation(s): 1. Cornell NanoScale Science and Technology Facility (CNF),
2. Department of Mechanical and Aerospace Engineering; Cornell University

Primary Source(s) of Research Funding: Cornell NanoScale Science and Technology Facility (CNF)

Contact: ober@cnf.cornell.edu, gd373@cornell.edu

Website: https://cnf.cornell.edu/

Primary CNF Tools Used: NanoScribe Photonic Professional GT2

Abstract:

Production of micro-scale devices, particularly for microfluidic applications, commonly require high aspect-ratio channels. The sub-micron resolution of the NanoScribe Photonic Professional GT2 allows arbitrarily complex channel designs to be fabricated with relative ease. However, these complex microfluidic channels present significant challenge in terms of post-print part development due to transport limitations of the developer. In this work, custom substrates were designed to increase developer transport, minimizing overall development time and increasing part quality due to decreased exposure to development chemicals. Additionally, through selection of compatible substrate materials it is possible to print directly to a matching material, resulting in a solid bond between the part and substrate.

Summary of Research:

Devices printed on the NanoScribe Photonic Professional GT2 require, at times, a lengthy development process consisting of soaking parts in propylene glycol methyl ether acetate (PGMEA) and isopropyl alcohol (IPA). In this process, PGMEA dissolves the bulk of the uncured acrylate resin left by the printing process, followed by a wash with IPA which removes the remaining PGMEA and resin. In high aspect ratio channels, this process is transport limited due in large part to the high viscosity of the liquid resin (>13,000 mPas at ambient temperature), which flows very slowly and mixes poorly with PGMEA without agitation. Increasing transport therefore will have a significant impact on decreasing development time. This will also help maintain the structural integrity of printed parts by minimizing swelling and ensuring overdevelopment does not occur.

Device design plays a large part in ensuring proper development; minimizing channel length and other bottlenecks in the design is critical. However, altering the substrate from the conventional silicon or borosilicate glass can yield significant dividends. Printing a device atop an open pore in the substrate offers a direct path for PGMEA development, of particular use for certain part orientations and designs. This can also reduce print time, as supports may no longer be required to raise a print from the surface or orient the part on its side. Figure 1 illustrates one such design, where a microfluidic structure is raised to allow for PGMEA transport via a set of supports which are later removed. By printing directly on a pore, this support structure is obviated and removes flow restrictions from below the structure.

A 25 mm × 25 mm × 4 mm substrate with integrated 1 mm diameter pore and microfluidic connector mount was designed, shown in Figures 2 and 3. The design for this substrate is available on the NanoScribe GT2 tool wiki, hosted by CNF under the section "Printing on Porous Substrates" [1]. Substrates were printed on three different resin-based printing systems: an Elegoo Mars 2 Pro with Elegoo Standard Transparent Resin, a low cost stereolithography (SLA) printer; a FormLabs Form 3 SLA printer with FormLabs Clear Resin, and a Carbon digital light synthesis (DLS) printer with Loctite 3D IND405 Clear Resin. In all cases, an acrylate resin was used to ensure compatibility with the printing process and subsequent development as the swelling may cause cracks to form in the substrate and device after the developers have evaporated. Additionally, the same 3D model was utilized, with print orientation varied based on the requirements of the printer.

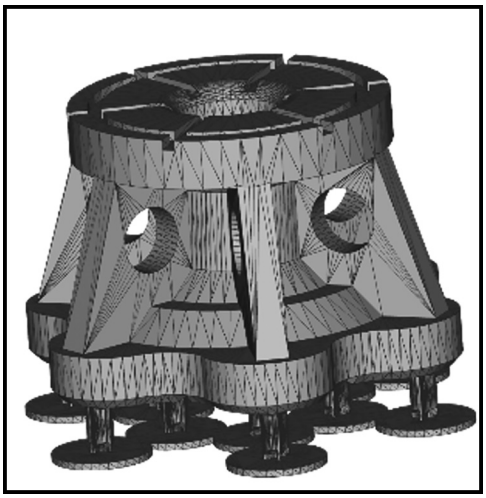

Figure 1: Original microfluidic device with standoffs for enhanced transport.

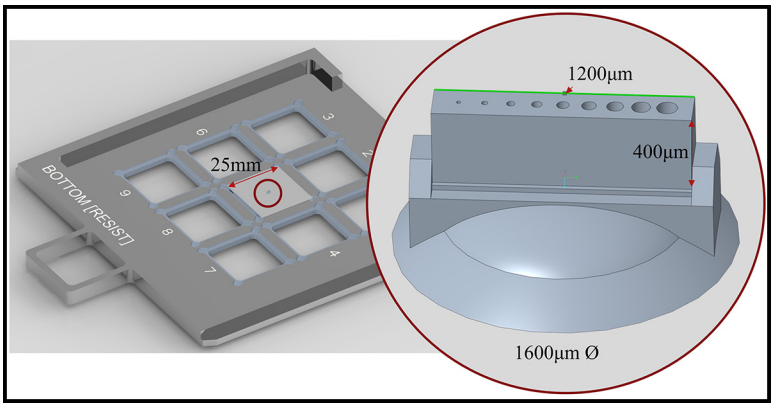

Figure 2: Model of substrate with 1 mm pore.

Figure 3: Model of printed microfluidic design on custom substrate.

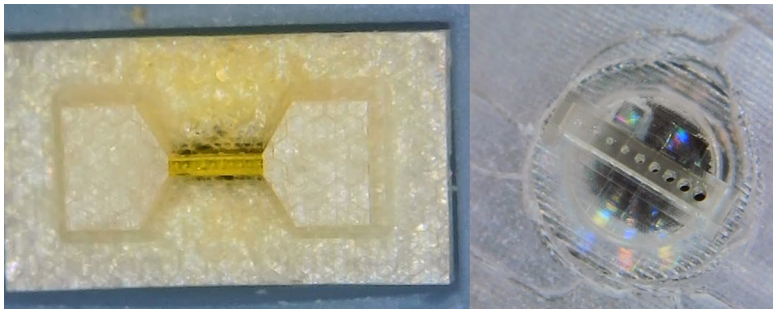

Figure 4: Two prints of a similar channel design illustrating overdevelopment of the old design (left) versus the well-developed porous substrate design.

After printing, the substrates were polished to a 3 µm surface finish then sonicated in IPA before use in the NanoScribe printer. The Elegoo Standard Transparent Resin had experienced minimal swelling and produced no defects due to the development process. The FormLabs Clear Resin swelled little and was acceptable for this process. The Loctite resin exhibited the most swelling during development with notable warping and is not suitable for fine parts, particularly if there are other printing options available.

Samples were printed with the 25x Medium Feature objective and IP-S resin. A microfluidic sample was developed in its standard configuration, then a modified version was reprinted on the porous substrate.

The standard sample required nearly 48 hours of development in PGMEA to attain clear channels, while experiencing massive structural issues due to PGMEA infiltration and swelling of the structure. The white, pillowy texture is characteristic of overdevelopment as the supporting shell-and-scaffold structure experienced significant PGMEA intrusion. The reprint on porous substrate was developed in one hour in PGMEA and 15 minutes in IPA. Due to this significantly shorter development time, device structure did not noticeably swell or overdevelop. A comparison of the two prints shows significant improvements in part quality, as seen in Figure 4. Further, this modification reduced print time from between 6 and 10 hours to just two hours since supports were no longer necessary and the part required less supporting structure for the same strength. Devices were subsequently pressure tested with both deionized water and 99% IPA with pressures of up to 345 mBar without leakage in the new design. Additional details regarding the use of these substrates is available to all users on the CNF User Wiki for Two-Photon Lithography.

References:

[1] "Two-photon Lithography - CNF User Wiki - Dashboard." https://confluence.cornell.edu/display/CNFUserWiki/Two-photon+Lithography.